NASA CR-174,636

A Reproduced Copy

OF

NASA CR-174,636

Reproduced for NASA

by the

NASA Scientific and Technical Information Facility

NASA Contractor Report 174636

Analysis and Testing of a New Method for Drop Size Measurement Using Laser Light Scatter Interferometry

W. D. Bachalo and M. J. Houser

Aerometrics, Inc.
Mountain View, California

August 1984

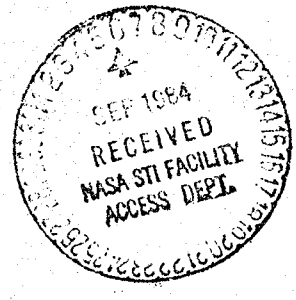

Prepared for

NATIONAL AERONAUTICS AND SPACE ADMINISTRATION
Lewis Research Center
Under Contract NAS3-23684

Table of Contents

This Page Intentionally Left Blank

NOMENCLATURE

$C(m, \theta)$	proportionality constant
E	electric field
I_{inc}	light beam intensity
I_o	light beam intensity at the measurement station
L	optical path length
N	number of drops per unit volume
P	power
Q_{ext}	extinction coefficient
Q_{scat}	light scattering coefficient
$S(\alpha, m, \theta)$	scattering amplitude functions
V	visibility
V_{min}, V_{max}	signal voltage levels
a	drop radius
d	drop diameter
d_b	laser beam diameter at transmitter lens
d_w	beam waist diameter
f	focal length
i_1, i_2	squares of the moduli of the amplitude functions
$j = \sqrt{-1}$	imaginary number
$k = 2\pi/\lambda$	wave number
m	refractive index
n	number of particles in size class
r	polar coordinate
s	beam separation at the transmitter lens
t	time
x, y	cartesian coordinates

$\alpha = \pi d/\lambda$	size parameter
γ	beam intersection angle
δ	fringe spacing
η	phase due to optical path length
θ	scattering angle
λ	laser wavelength
π	3.142
σ	combined phase due to focal lines, optical path, and reflection
τ	light ray incident angle to the surface tangent
τ'	refracted ray
ϕ	phase shift of the Doppler signals

1.0 INTRODUCTION

A research program was conducted to evaluate an innovative concept for spray drop size and velocity characterization. This program was motivated by the increasing demands on diagnostic techniques which have accelerated with the need to form spray drops having controlled size distributions, spray patterns, and mass flow rates. The goal of this program is to develop an instrument for fuel spray combustion applications. However, the required capability of efficiently and accurately characterizing sprays is associated with a much larger range of technologies. These applications include coal-oil and coal-water slurry combustion, nuclear reactor safety, aircraft icing, agricultural sprays, meteorology and a variety of industrial processes.

The development of advanced laser-based instrumentation remains of importance to the progress of experimental research and predictive code development in fuel spray combustion. Increased knowledge and understanding of the fluid dynamics and combustion chemistry are required in the development of aircraft engine combustors to enable continuous and efficient burning of fuel at high rates with a minimum of soot and other pollutant formation. Presently there is considerable interest in obtaining measurements of the fuel and air motions within the spray droplet combustors. It is known that the turbulent motions influence the reactions by increasing the oxygen supply to the burning fuel. The relative velocities between the gas phase and liquid droplets not only provides oxygen to the burning droplet but also serves to remove the products of combustion and hence, affects the evaporation and burning rates and the pollutant formation. Thus, the droplet size distribution and velocity are important data to be obtained when characterizing the combustion process.

Basic research has also been conducted on two-phase turbulent jets[1,2,3,4] to furnish a basis for the development of predictive codes that may ultimately describe the fluid dynamics of spray combustion. This work has revealed that the turbulence structure of the continuous phase is altered by the presence of the dispersed phase. As may be expected, the dispersed phase reduces the turbulence spectral intensity, in particular the higher frequencies, since the dispersed phase droplets do not track the turbulent eddy fluctuations and thus, increase the dissipation of turbulent kinetic energy. Experimental investigations

have been carried out to measure the turbulence characteristics with solid monodispersed particulate. The need to obtain a complete data base using monodisperse and polydisperse liquid droplets requires a reliable means for drop size and velocity measurement and for the separation of the gas phase and liquid droplet velocity measurements.

The need for simultaneous size and velocity measurements has been recognized even for the general characterization of sprays. This is especially true when studying nozzles that generate droplets that are moving at a relatively high velocity and subsequently relax to the ambient flow speed in accord with their initial momentum. The differing flux of the various size classes can affect the measured size distributions depending on the method of measurement.

In general, droplet sizing imposes unique constraints upon the techniques that may be utilized. Droplets are deformable, break up under aerodynamic forces and collisions with probes, contaminate surfaces, and are often present at high number densities. Sampling and other material probe methods are therefore less desirable for implementation in spray measurements. Optical methods consisting of imaging and laser light scatter detection have been applied with varying degrees of success. The relative success of a method is largely dependent upon the measurement environment, droplet size and number density, type of material forming the droplets, and other physical constraints of the test apparatus. Instrument limitations are dependent upon the physical concepts incorporated into the measurement device and how these concepts are affected by interaction with the surrounding spray, aerodynamic and temperature fields. Techniques that have proven reliable in one measurement situation have produced erroneous results in others.

Because of the high droplet number densities involved, most light scattering methods classified as single particle counter systems will not function properly in spray environments. Basic methods utilizing absolute light scattering intensity measurements will experience significant errors due to partial extinction of the laser beam and scattered light. For these reasons, the small angle scatter detection methods developed by Dobbins et al.[5] and Swithenbank et al.[6] have been favorably received. Unfortunately, instruments based on these concepts can only measure the Sauter mean diameter (SMD) directly. Furthermore, these measurements are made over the entire exposed path of the laser beam

which results in poor spatial resolution. The methods cannot produce information on the droplet number density or the velocity.

Simultaneous measurement of the droplet size and velocity has led to the combination of the laser Doppler velocimeter (LDV) with particle sizing methods. Particle sizing interferometry developed by Farmer[7] was a significant attempt in achieving this goal. The method utilized a standard LDV optical arrangement with on-axis light scatter detection. Signal visibility was processed to obtain information relatable to the particle diameter. The method was however, limited to very low number density particle or droplet environments. Yule, et al[8] attempted to make simultaneous size and velocity measurements using an LDV with small off-axis angle scatter detection. The droplet size information was obtained from the amplitude of the scattered light intensity. The difficulties involved with the Gaussian beam intensity distribution notwithstanding, the measurements were also affected by the partial extinction of the laser beams and the scattered light.

Bachalo[9] described a method that eliminated many of the aforementioned difficulties by producing a rigorous analysis of the dual beam laser light scatter for large off-axis receiver angles. By using large angle light scatter detection, the measurement region could be reduced by as much as two orders of magnitude compared with the on-axis approach. This contribution suggested that the measurement of the size and velocity of individual droplets might be possible in dense sprays. Use of the light scattered by reflection and refraction allowed the measurement of droplets as large as several millimeters in diameter.

The Droplet Sizing Interferometer based on the technique proved to be successful in producing droplet size and velocity and size-velocity correlations measurements under limited spray conditions. However, because of the signal processing methods used, the system had some serious limitations. These included the need for extremely careful alignment, a size range sensitivity of a decade or less with reduced size sensitivity at the small size end of the range, a narrow Doppler frequency response range and sensitivity to laser beam quality and relative intensity of the two beams.

Because of the significant potential advantages of the light scattering interferometry method, a new means for processing the interference information was derived. This

innovation promised to increase the dynamic range of the system while reducing the possibility of measurement error resulting from imperfect alignment or beam intensity differences at the probe volume. The concept resulted in a linear response to the drop size with a relatively uniform sensitivity over the entire measurement range. A measurement range of over a factor of 30 can be attained while a factor of 100 may be possible without optical adjustment but with only a change in photodetector gain.

In the following sections, a theoretical description of the concept is presented and the experimental setup of the device is described. The test procedures used to evaluate the method are outlined and test results are presented.

2.0 THEORETICAL DESCRIPTION

2.1 Light Scattering Theory

The scattering of light by homogeneous dielectric spheres of arbitrary size is described exactly by the well-known Lorenz-Mie theory. However, even with large computers, the computation time required to calculate the scattering coefficients for a range of drop sizes can be prohibitive. The number of terms needed to be computed in the series solution is proportional to the size parameter $\alpha = \pi d/\lambda$. Fortunately, for drop sizes greater than the light wavelength λ, simpler asymptotic theories may be used. For spherical scatterers that can be regarded as small spherical lenses or mirrors, the geometrical optics methods produce accurate results.

van de Hulst[10] showed that for spheres much larger than the light wavelength and with refractive index sufficiently different from the surroundings, the amplitude functions derived from the geometrical optics approach were, in the asymptotic limit, equal to the Mie amplitude functions. Comparisons have been made to the exact Mie theory by a number of researchers[11,12] to demonstrate the accuracy of the geometrical optics methods. Very good agreement was demonstrated by Glantschnig and Chen[12] for drops as small as 5 micrometers. van de Hulst demonstrated that for $\alpha > 10$, the scattering of light can be separated into the simplified theories of diffraction, refraction, and reflection.

Scattered Intensity

Light scattered by diffraction which is described by the following expression

$$S_{diff}(\alpha, \theta) = \frac{\alpha^2}{4\pi}\lambda\left[\frac{J_1(\alpha \sin\theta)}{\alpha \sin\theta}\right] \qquad (1)$$

where J_1 is the Bessel's function and θ is the scattering angle is concentrated in a lobe centered about the transmitted beam. This forward scattered light becomes more intense by the diameter squared and smaller in angular distribution with increasing drop size. Hodkinson and Greenleaver[11] have shown that for $\alpha > 15$, diffraction becomes insignificant at scattering angles greater than 10°. For spheres of refractive index $m = 1.5$ and diameters as small as 2 micrometers, diffractive scatter is less than 10% of the total light scattered at 45°. Thus, the light scattered by diffraction can be avoided when desired, by proper placement of the receiver.

Light scattered by reflection and refraction is best described in terms of rays and the use of the simple laws of reflection and refraction. When a ray impinges on the surface of a transparent sphere it produces a reflected and refracted ray, figure 1. The direction of the refracted ray follows from Snell's law:

$$\cos\tau = m\cos\tau' \tag{2}$$

where τ and τ' are the angles between the surface tangent and the incident and refracted rays, respectively. The partitioning of the energy into the two rays follows from the Fresnel coefficients.

The emerging rays are characterized by two parameters, the angle τ of the incident ray and the integer p of the interface from which it emerges. That is, $p = 0$ for the first surface reflection, $p = 1$ for the transmitted ray and $p = 2$ for the ray emerging after one internal reflection. The energy in the remaining reflections is insignificant. The angle between the incident ray and the p^{th} emergent ray is given by

$$\theta = 2(p\tau' - \tau) \tag{3}$$

The fraction of the incident intensity contained in the emergent rays can be obtained from the Fresnel coefficients. The details of derivation of the closed form θ-dependent intensity functions are given in Glantschnig and Chen and only the results will be quoted here.

In the notation of van de Hulst, the scattered light is described in terms of two amplitude functions, $S_1(\alpha, m, \theta)$ and $S_2(\alpha, m, \theta)$ for the perpendicular (to the scattering plane) and parallel incident polarizations, respectively. van de Hulst demonstrated that a large sphere scatters over 90% of the incident light in the forward direction with 99.5% of the forward scattered light emerging from the first two interfaces ($p = 0$ and $p = 1$). Thus, only the first two terms of the series describing the rays emerging from the various interfaces need be considered for most practical applications.

Glantschnig and Chen obtained the following expressions for the amplitude function

describing the rays reflected from the first surface of the sphere:

$$S_1^{(1)}(\alpha, m, \theta) = \alpha \frac{\sin\frac{\theta}{2} - \sqrt{m^2 - \cos^2\frac{\theta}{2}}}{\sin\frac{\theta}{2} + \sqrt{m^2 - \cos^2\frac{\theta}{2}}} \frac{1}{2} \exp\left[j\left(\frac{\pi}{2} + 2\alpha \sin\frac{\theta}{2}\right)\right] \quad . \tag{4}$$

$$S_2^{(1)}(\alpha, m, \theta) = \alpha \frac{m^2 \sin\frac{\theta}{2} - \sqrt{m^2 - \cos^2\frac{\theta}{2}}}{m^2 \sin\frac{\theta}{2} + \sqrt{m^2 - \cos^2\frac{\theta}{2}}} \frac{1}{2} \exp\left[j\left(\frac{\pi}{2} + 2\alpha \sin\frac{\theta}{2}\right)\right] \quad . \tag{5}$$

where superscript 1 implies the $p = 0$ reflection and subscripts 1 and 2 represent the perpendicular and parallel polarizations respectively. The amplitude functions for the rays emerging from the second surface after refraction by the sphere are given as follows:

$$S_1^{(2)}(\alpha, m, \theta) = \alpha\left[1 - \left(\frac{1 + m^2 - 2m\cos\frac{\theta}{2}}{1 - m^2}\right)^2\right]\sqrt{\frac{m^2 \sin\frac{\theta}{2}\left(m\cos\frac{\theta}{2} - 1\right)\left(m - \cos\frac{\theta}{2}\right)}{2\sin\theta\left(1 + m^2 - 2m\cos\frac{\theta}{2}\right)^2}} \times \exp\left[j\left(\frac{3\pi}{2} - 2\alpha\sqrt{1 + m^2 - 2m\cos\frac{\theta}{2}}\right)\right] \quad . \tag{6}$$

$$S_2^{(2)}(\alpha, m, \theta) = \alpha\left[1 - \left(\frac{(1 + m^2)\cos\frac{\theta}{2} - 2m}{(m^2 - 1)\cos\frac{\theta}{2}}\right)^2\right]\sqrt{\frac{m^2 \sin\frac{\theta}{2}\left(m\cos\frac{\theta}{2} - 1\right)\left(m - \cos\frac{\theta}{2}\right)}{2\sin\theta\left(1 + m^2 - 2m\cos\frac{\theta}{2}\right)^2}} \times \exp\left[j\left(\frac{3\pi}{2} - 2\alpha\sqrt{1 + m^2 - 2m\cos\frac{\theta}{2}}\right)\right] \quad . \tag{7}$$

Summing the amplitude functions, the total for forward light scattering is given as

$$S_j(\alpha, m, \theta) = S_{diff}(\alpha, \theta) + S_j^1(\alpha, m, \theta) + S_j^2(\alpha, m, \theta) \qquad j = 1, 2 \tag{8}$$

The dimensionless intensities i_j are simply

$$i_j(\alpha, m, \theta) = |S_j(\alpha, m, \theta)|^2 \tag{9}$$

These expressions produce accurate results with the exception of scattering at grazing or nearly grazing incidence and for scattering into the rainbow angles as indicated by van de Hulst. The geometrical optics results can be used for values of $\alpha \geq 15$ depending upon the information (what scattering angles) and accuracy required. Comparisons of an example calculation with Mie theory (from Ref. 12) are shown in figure 2. The agreement for the 5μm diameter droplets is very good even though this is near the minimum size wherein the geometrical optics approximation applies.

For spheres large enough ($d > 3\mu$m) to satisfy the above criteria, the scattered light intensity appears as an obvious means for size analysis. The square of the diameter of the spherical scatterer can be assumed to be proportional to the scattered light intensity,

$$I_{scat}(d, m, \theta) = C(m, \theta) \cdot d^2 \tag{10}$$

This relationship is correct provided that the receiver $f/no.$ is small enough to form an average over the angular fluctuations resulting from interference between the reflected ($p = 0$) and refracted ($p = 1$) light. The measured light intensity is also dependent upon the incident intensity I_o which is multipled by the scattering coefficient, Q_{scat}. In practice, the optical collection efficiency and losses in the system are determined by calibrations using spherical particles or drops of known size. Unfortunately in realistic droplet environments, the droplets will attenuate the transmitted beams and the scattered light by an indeterminate amount.

For example, the light intensity scattered by a cloud of drops is

$$Q_{scat,N} = \sum_{i=1}^{k} n_i(d_i) I_{scat}(m, \theta, d_i) \tag{11}$$

where the n_i are the number of particles of size d_i. The loss of power due to transmission of the beam through a droplet field of path length, L is given by the well known Lambert-Beer law as

$$dP = -k_{ext} I A dx \tag{12}$$

and the integration over the path length L gives

$$I = I_{inc} \exp(-\int_0^L k_{ext} dx) \tag{13}$$

where I_{inc} is the incident intensity where $x = 0$. It is known that for large α the extinction coefficient approaches the value of 2 asymptotically. That is,

$$\lim_{\alpha \to \infty} Q_{ext} = 2 \tag{14}$$

This is often referred to as the extinction anomaly since large spheres would be expected to block the light falling on there cross-sectional area. However diffraction which is an edge effect also scatters light proportional to the drop cross-sectional area. In the absence of any absorption,

$$\begin{aligned} k_{ext} &= N Q_{ext} \pi a^2 \\ &= 2N\pi a^2 \end{aligned} \tag{15}$$

where a is the average drop radius in the field. Hence,

$$I_o = I_{inc} \exp(-2NL\pi a^2) \tag{16}$$

where N is the number of droplets per unit volume and L is the optical path length through the spray. For example, a spray with a mean drop size of 50μm at a number density of 100 drops/cc and a width of 20 cm will have an attenuation of $I_o/I_{inc} = 0.92$. Assuming that Q_{ecat} is proportional to d^2, the error in the determination of d is approximately 4%. At a droplet concentration of 500 drops/cc, the measured drop size would be 18% smaller than it actually was barring any other attenuations in the optical path. The number densities used in these examples are not atypical of those found in actual sprays. Thus, the simple use of scattered light intensity may not be a reliable method for measuring sprays. Even with frequent calibrations, these uncertainties due to attenuation by drops in the beam will occur.

Phase Due to Optical Path

The light rays emerging from the sphere will have different path lengths depending upon the angle of scatter and the path lengths through the sphere. For this reason, the

intensities of the outgoing beams cannot be added directly. The beams which all originated from the same coherent incident wave must have their complex amplitudes added and the squared modulus then becomes the correct intensity.

In order to compute the phases from ray optics, van de Hulst references the actual ray to a hypothetical ray scattered without a phase lag at the center of the sphere. Neglecting phase shifts of π at reflection and phase shifts of $\pi/2$ at focal lines (all of which cancel from the subsequent analysis), a simple geometric analysis results in the expression

$$\eta = 2\alpha(\sin\tau - pm\sin\tau') \tag{17}$$

for the phase shift with respect to the reference ray. It is of interest to note that the phase is directly proportional to $\alpha = \frac{\pi d}{\lambda}$ which implies that the number of extrema in the scattering pattern is also proportional to the dimensionless size, α. The change in phase which is independent of the incident intensity or scattering amplitudes but is directly proportional to the drop diameter is a more practical means for obtaining the size information.

Dual Beam Light Scattering

One approach for extracting size information from the phase shift is to utilize the dual beam scattering arrangement of the familiar laser Doppler velocimeter (LDV), figure 3. Assuming linearly polarized light, the amplitude functions associated with scattering from beams 1 and 2 are

$$S_{11}(m,\theta,d) = \sqrt{i_1}\exp(j\sigma_1) \tag{18}$$

$$S_{12}(m,\theta,d) = \sqrt{i_2}\exp(j\sigma_2) \tag{19}$$

where the double subscript indicates only polarization 1 is considered, j is the imaginary value $j^2 = -1$ and $\sigma = \eta$ neglecting phases shifts of π due to reflection, $\pi/2$ due to focal lines and the Fresnel coefficients. When a spherical particle passes through the intersection of the two beams, it will scatter light from each beam as if the other beam was not there. Thus, the scattered light waves may be described as

$$E_1(m,\theta,d) = S_{11}(m,\theta,d)\frac{\exp(-jkr + j\omega_1 t)}{jkr} \tag{20}$$

$$E_2(m,\theta,d) = S_{12}(m,\theta,d)\frac{\exp(-jkr + j\omega_2 t)}{jkr} \tag{21}$$

The total scatter is obtained by summing the complex amplitudes from each beam and then determining the intensity which is

$$I(m,\theta,d) = \left(|E_1|^2 + |E_2|^2 + 2|E_1||E_2|\cos\sigma\right) \tag{22}$$

were σ is the phase difference between the scattered fields. In this expression, the cross product term $2|E_1||E_2|\cos\sigma$ corresponds to the sinusoidal intensity variation of the fringe pattern while the $|E_1|^2 + |E_2|^2$ terms are the d.c. or pedestal components. The visibility of the scattered fringe pattern is simply equal to the ratio of these two terms.

$$V = \frac{2|E_1||E_2|\cos\sigma}{|E_1|^2 + |E_2|^2} \tag{23}$$

Confusion can occur here by the use of the terms visibility and signal visibility. In the former case, Michelson's definition is implied which is a measure of the distinctness of the fringes formed in the space surrounding the drop, figure 4. If a *point* detector was moved normal to the resultant fringe pattern, a signal proportional to the local light intensity would be produced and the visibility of the resultant sinusoidal signal would be

$$V = \frac{V_{\max} - V_{\min}}{V_{\max} + V_{\min}} \tag{24}$$

The *signal visibility* is the relative modulation of the signal received through the detection optics and photodetector. This is usually produced by the integration of the scattered fringe pattern over the area of the receiver lens. In general, the signal visibility depends on the receiver aperture, drop size, the beam intersection angle, and light wavelength as

well as other parameters and will always be less than or equal to the scattered interference fringe visibility.

Since the rays from beams 1 and 2 intersect at a small angle, $\gamma(< 10°)$, at the sphere, the scattering angles θ_1 and θ_2 for these pairs of rays reaching a common point in space and interfering are approximately equal. Thus, the amplitude functions S_1 and S_2 are also approximately equal. From equations 20, 21, and 23, it follows that the visibility of the fringe pattern is approximately unity. The spatial frequency of the fringe pattern is determined by the relative phase difference, σ of the interfering light waves scattered from beams 1 and 2.

Signal visibility has been used as a means for determining the drop size [7]. When the drop moves through the intersecting laser beams, the fringe pattern that is produced appears to move at the Doppler difference frequency. The Doppler difference frequency is a function of the beam intersection angle, light wavelength, and the velocity of the drop. The spatial frequency of the fringe pattern is dependent upon the angle of observation, drop index of refraction, beam intersection angle, laser wavelength and the drop diameter. Placement of a receiver lens to collect the scattered light will produce a Doppler burst signal as shown in figure 5. The lens, in effect, acts as a length scale to measure the spatial frequency of the scattered fringe pattern. Integration of the fringe pattern over the receiver aperture produces a Doppler burst signal with a signal visibility that may be related to the drop size. This relationship is shown in figure 6.

Although the method based on measuring the signal visibility partially eliminated the problems associated with intensity measurements, provided a means for the simultaneous measurement of the drop size and velocity, and did this with high spatial resolution, it has several shortcomings. As previously mentioned, the visibility of the scattered fringe pattern will be equal to unity if the scattered intensities from each beam are equal. Since the measured signal visibility depends on this being true, the incident laser beams must be of equal intensity in addition to having the same linear polarization direction and being coherent. These requirements may be frustrated by optical imperfections and alternate attenuations of the beams by large drops. Because of the Bessels function relationship between the measured signal visibility and the dimensionless drop size, the error produced

can be relatively large at the small size end of the measurement range. Another difficulty associated with the instrument response function is the limited size range of a factor of 10 or less. Typical drop size distributions extend over a factor of 30 or greater. Because of the need to have equal intensities from each beam incident upon the drop, the alignment of the system is also very critical.

2.2 Phase/Doppler Spray Analyzer Technique

As aforementioned, the spatial frequency of the interference fringe pattern produced by the scattered light is linearly related to the drop size. The mathematical description of the interference pattern which includes the effects of all of the optical parameters, is then required before this information may be utilized. With the complete theoretical description of the scattered fringe patterns for the appropriate parameters, there is no longer any need to calibrate the system for each measurement task. The drop size measurement can then be obtained from the accurate measurement of the spatial frequency of the interference fringe pattern.

The theoretical description of the fringe pattern was derived and software was generated to compute the fringe patterns at any selected optical parameters and to plot the resultant interference fringe pattern. Three scattering regions of practical interest were considered: forward scatter $10° \leq \theta \leq 50°$, backscatter $130° \leq \theta \leq 170°$, and $\theta = 90°$ where θ is measured with respect to the transmitted beam direction. Light scattering by a combination of refraction and reflection at similar intensity will occur at some angles and under certain parametric conditions. Where this occurs, the spatial fringe pattern is no longer a pure sinusoidal intensity variation because of the multi-component scattering interference. That is, additional interference between the refracted and reflected rays will occur and produce significant errors. Such errors can be minimized or eliminated with the proper selection of detection and processing methods. The computational schemes were able to accurately represent these phenomena graphically and thus, allowed the development of the optics to avoid these possible error sources.

An example of the computed interference fringe pattern is given in figure 7. The sinusoidal fringe pattern was computed for a plane normal to the beam directions. Only

the upper half of the symmetric fringe pattern was reproduced. As observable on the figure, the fringes are hyperbolic curves showing a decreasing spatial frequency with distance from the beam axis at $x = 0, y = 0$. The pattern is also symmetric about $x = 0$. Thus, the spatial frequency of the fringe pattern is dependent on where the measurement is made.

Measurement of the fringe pattern would be relatively easy if the fringes were of relatively high intensity and of low temporal frequency. Unfortunately, the temporal frequency of the fringe pattern is essentially the Doppler difference frequency that will vary according to the speed of the drop. This frequency may be as high as 2 MHz in spray environments. The scattered light intensities will be low and will vary over several orders of magnitude. A receiver lens and either photomultiplier tubes or solid state detectors are required to provide the necessary sensitivity.

The scheme used to measure the spatial frequency of the scattered fringe pattern requires the use of two or more detectors separated by fixed spacings. As the drop passes through the beam intersection region the fringe pattern appears to move past the receiver at the Doppler difference frequency. A Doppler burst signal similar to that shown in figure 5 will be produced by each detector but with a phase shift between them as illustrated in figure 8. The signals in this figure have been high pass filtered to remove the pedestal component. The phase shift is then determined by measuring the time between the zero crossings of the signals from detector 1 and 2 and dividing by the measured Doppler period. That is,

$$\phi_{1-2} = \frac{\tau_{1-2}}{\tau_D} \times 360^\circ \tag{25}$$

where the measurements are averaged over all the cycles in the Doppler burst signal. Measurements of the phase shift are then related to the droplet size using the linear relationships shown in figure 9.

In figure 9, the effect of changing the optical parameters which include the laser beam intersection angle, collection angle, drop index of refraction, laser wavelength, and scattering component detected is to simply change the slopes of the linear response curves. That is, only the size scale is changed for the same range of phase angles since the curves all must pass through the origin.

Three detectors are required to ensure that measurement ambiguity does not occur. When measuring polydisperse sprays without knowing the approximate size a priori, phase shifts of greater than 360° could occur. Such occurrences would be measured as being less than 360°. The third detector provides a logical test to identify and eliminate such uncertainties. Proper selection of the detector spacings also provides two sensitivity ranges shown as curves ϕ_{1-2} and ϕ_{1-3} on figure 9. The two phase measurements will allow the additional testing of the measurements in the overlap region and extends the size range sensitivity at one optical setting to a factor of approximately 100.

The dynamic range which refers to the ultimate size range measurable at one setting including the range of the detectors is somewhat less than 100. Because the drops scatter light approximately in proportion to their diameter squared, the detector would require a dynamic response over a factor of 10^4 or greater. A factor of 10^3 is realistic. However, the detector gain can be easily set to select the optimum sensitivity without requiring any optical adjustments and realignment.

Thus, the method has several potential advantages for obtaining drop size and velocity data. Because of the range of validity of the scattering analysis used, the overall size range is 3 micrometers to 2000 provided the drops remain spherical. Both the drop size and its velocity are measured simultaneously. This capability is useful in providing a complete description of the spray drop size distribution (including both the spatial and temporal distributions). Measurements of two-phase turbulent flows which requires the determination of drop size-velocity correlations and the gas phase velocity based on small particles is an important capability of the method. With the use of highly focused beams and off-axis scatter detection, these measurements can be made with very high spatial resolution.

In the following sections, a summary of the experimental evaluations of the method are discussed along with a presentation of the results.

3.0 EXPERIMENT

The experimental effort was directed toward the verification of the theoretical analysis, evaluation of the phase processing method, and investigation into signal quality effects. The early stage of the experiments was concerned with validating the predicted signal phase shifts. This validation was necessary before any effort was expended on signal processor design and development which would be a major task in itself. As a result, initial phase measurements were obtained from individual oscilloscope traces of the detector outputs. Although tedious, this method proved satisfactory in providing the necessary verification to justify continuation of the experiments. Following the successful validation of the phase shift theory for a limited number of cases, attention was given to the development of an electronic signal processing method. A breadboard processor was designed and constructed allowing the accumulation of large data records at a relatively fast rate. The addition of the signal processor permitted further verification of the theory over a wide range of system parameters. Also investigated was the effect of signal degradation on the measured phase shift. Sources of signal degradation known to adversely affect similar droplet sizing schemes were examined to determine their effect on the phase shift method.

3.1 Description of the Apparatus

The basic hardware and equipment needed for the experimental phase of the project included: transmitting optics, receiving optics with detectors, electronic signal amplifiers, filters, signal processor, oscilloscope, data management system, and a droplet source. Although the configuration of the system changed at times and components were added or omitted as necessary, the basic arrangement remained the same. A photograph of the apparatus is given in figure 10 and a description of the components follows.

Optics

The optics are divided into a transmitter and receiver package. Each was assembled independently on an optical rail which allowed reconfiguration of the light scatter geometry to any desired collection angle. The primary configuration was the arrangement shown in figure 11 which was the 30° off-axis forward scatter collection geometry. A majority of the data was obtained with this arrangement.

The transmitter package consisted of a low power He-Ne laser operating at a wavelength of 0.6328 micrometers, a beamsplitter (BS) which allowed for a variable beam separation, and transmitter lens (L1) with focal lengths of either 220mm or 100mm. The beamsplitter produced two parallel beams which were caused to intersect by the transmitting lens. The beam crossover is the point at which measurements are made and is referred to as the 'probe volume'. Interference between the two incident laser beams occurs at the probe volume resulting in the formation of planar interference fringes parallel to each other and separated by a distance known as the fringe spacing given by:

$$\delta = \frac{\lambda}{2\sin\left(\frac{\gamma}{2}\right)} \approx \frac{\lambda f}{s} \tag{26}$$

where δ = fringe spacing, λ = laser wavelength, γ = beam intersection angle, f = transmitter lens focal length, and s = beam separation at lens. The number of fringes within the probe volume is given by:

$$N = \frac{d_w}{\delta} \tag{27}$$

$$d_w = \frac{4\lambda f}{\pi d_b} \tag{28}$$

where N = number of fringes, d_w = beam waist diameter, and d_b = laser beam diameter at transmitter lens. Variations in the above values are obtained by adjustment of the beam separation, s , or transmitter lens focal length, f.

The receiver package was comprised of a lens assembly (L2, L3) which collected light scattered by droplets within the probe volume and focused it onto the pinhole. The pinhole acted as a spatial filter blocking the light scattered from other than the probe volume. Light which passed the pinhole was directed by mirrors M1 and M2 to detectors D1 and D2. The mirrors were adjusted so that light from different, well-defined areas of the receiver lens was directed to either D1 or D2. This resulted in an effective detector separation across the face of the receiver aperture. The separation was variable and referred to as

the slit separation. The receiver package was modular and thus, could be placed at the selected angle of collection, θ, measured from the bisector of the intersecting laser beams (transmitter axis).

Electronics and Data Management

Although physically a part of the receiver package, the detectors deserve additional consideration. Solid state silicon photodiodes were initially selected to act as detectors. The quantum efficiency of silicon photocells can approach 90% at the HeNe laser wavelength. The photodiodes are rugged, easily manageable, require only nominal (-15 VDC) operating voltages, and can be obtained with integral pre-amplifiers. A good deal of time was spent developing silicon photodiodes to act as detectors for the phase measurement system. Unfortunately, background noise levels could not be lowered enough to provide the required signal dynamic range of which the instrument was capable. It is felt that silicon photodiodes or lower noise silicon avalanche photodiodes could be engineered to perform satisfactorily but such development was beyond the scope of this effort. A decision was made to employ photomultiplier tubes (PMT) as signal detectors for the duration of the experiments. Although more fragile and bulky than solid state devices, PMT's exhibit almost negligible background noise levels and provide enough signal gain to overshadow their lack of quantum efficiency. They also provided a convenient means of signal level selection by adjustment of the PMT high voltage.

Additional instrumentation utilized in the experiments included variable high pass filters and logarithmic amplifiers for each of the two channels. The high pass filters removed the pedestal component from the burst signals while the log amps provided compression of the wide range of signal amplitudes. A dual channel oscilloscope was used to monitor the signals at various points along the signal conditioning path.

As mentioned, initial phase measurements were obtained from individual oscilloscope traces which were manually analyzed (figure 12). As confidence in the theory increased, several automatic processing schemes were considered. Among them were analog phase determination using a signal mixer, cross-correlation techniques, signal digitizing using analog-to-digital converters, and digital processing schemes. The close association of the

phase technique with conventional LDV systems provided a basis of existing digital signal processing technology. The addition of phase determination circuitry to this type of processing scheme was deemed most suitable and straightforward. A prototype processor was developed which incorporated two parallel channels of Doppler period determination and a relative phase measurement. Signal validation included amplitude comparison (threshold and conventional three-level logic) circuitry designed to eliminate erroneous signal scoring. The processor also included the 'variable N' capability. The number of fringe crossings needed to produce a valid signal was not fixed as some processing schemes require. The minimum number of cycles was user selectable, but the processor was designed to utilize all available signal cycles in its period and phase determination. This capability guarantees that the most accurate central cycles of each signal burst are included in the measurement. Subsequent testing proved this to be a highly desirable feature of the processor. Individual signal period and phase determinations were output by the processor to the data acquisition system.

An IBM PC microcomputer was programmed to accept input and manipulate data from the signal processor. Calculations of droplet size and velocity from the raw phase and period data were executed by the computer. A real time display of the size histogram was also provided by the computer. Upon completion of data acquisition, linear mean diameter and, when appropriate, Sauter mean diameter were calculated for the accumulated data. An accompanying printer provided a hard copy record of the reduced data.

Drop Sources

Drops necessary to evaluate the system and verify the theory were generated from three different devices.

The Berglund-Liu generator[13] device produces a stream of monodisperse drops. The range of useful drop sizes obtainable was roughly 90 to 160 micrometers which often depended upon the operating peculiarities of the generator. Since the device was operated off the manufacturers recommended conditions, the drop stream would sometimes become unstable producing a scattering of drop sizes instead of the desired monodispersity. Not only could this device produce a known-sized, variable, monodisperse drop field, but the

streamwise nature of the drops also allowed them to be selectively directed through specific parts of the probe volume. The Berglund-Liu was the only drop size standard used for the phase measurement experiments.

The highly controllable nature of the Berglund-Liu device was necessary for verification of the theory, but did not represent the true environment of most drop fields. Polydispersions of drop sizes and a certain randomness of drop trajectory, velocity, and arrival at the probe volume are more characteristic of a spray environment. Unfortunately, there are no 'calibrated' drop sources of the type described, due in part, to the lack of instrumentation capable of performing such calibrations.

To better simulate the actual spray environment, several spray nozzles were used. The water supply used in the laboratory had a maximum line pressure of 80 psi. The pressure was regulated to produce varying spray characteristics. The nozzles used were low to moderate flow rate (.5 to several gallons per hours), solid cone type. Garden variety nozzles were sometimes used to produce larger drops in a hollow cone spray pattern.

A spinning disc atomizer was utilized for one set of tests. This device is used for room humidification and is known to generate very small ($\sim$ 4-30 μm) drops in a very narrow distribution. Both of these features were used in estimating the performance of the phase measurement system.

3.2 Experimental Verification of the Theory

Experimental data were obtained to validate the theoretical predictions. Of particular importance was the verification of the linear relationship between measured signal phase shift and drop size. Parameters other than drop size which were known to affect the measurement include fringe spacing, receiving lens geometry, and receiving angle. Each of these parameters was investigated individually. The system response to more realistic spray environments was tested using a series of spray nozzles and the spinning disc atomizer.

Droplet Size Variations

The system was aligned into the 30° forward scatter configuration (figure 11). The monodisperse droplet generator was the drop source. The generator could be tuned over a range of operating frequencies to produce drop sizes from 90 to 160 micrometers in

diameter. This narrow spread in drop diameters was limited by the droplet generator and represented only a small part of the dynamic range of the instrument. To test the method at both the upper and lower ends of the size range, the effective detector separation was changed to double the maximum drop size thus lowering the phase shift for the drops produced by the monodisperse generator. The individual data listings are given in figures 13 thru 18. This size data has been converted to phase angle and is compared to the theory in figure 19 showing excellent agreement.

Fringe Spacing Variations

The resultant size range sensitivity for the phase measurement instrument is a function of fringe spacing, detector separation, receiver collection angle, and drop index of refraction. The fringe spacing was changed with the accompanying size range variation in the next series of tests. Each change in fringe spacing also incurred a proportional change in signal frequency, number of fringes, and signal amplitude. Again, the Berglund-Liu monodisperse generator was used to produce drops of consistent size and velocity so that the above changes could be anticipated as the fringe spacing was varied. A change in signal frequency required a similar change in the high pass filter cutoff while a variation in signal amplitude required a detector gain adjustment. Compensation for the change in number of fringes also affected the high pass filter setting. Every attempt was made to minimize the effect of these secondary factors during these tests. The fringe spacing was varied from 10.7 to 44.9 micrometers by adjustment of the beam separation at the beam splitter. Data listings for one representative test are given in figures 20 thru 23. These data are converted to phase angle and plotted against theory in figure 24. Further substantiating data from similar tests are also shown.

Lens Geometry Variations

Scattered light intercepted by the receiver lens was selectively directed to each of the two detectors employed in the experiments. This was accomplished by masking the receiver lens into two separate regions such that mirrors could be used to separate and direct light to respective detectors. Since the receiver masking determined the effective detector separation, this parameter was very important in fixing the size sensitivity of the

instrument. In fact, size sensitivity is linear with effective detector spacing. Thus, size sensitivity could be conveniently varied by changing the receiver lens masking without changing other signal characteristics.

To test the response of the instrument to effective detector spacing, a series of receiver masking geometries was employed. The centroids of the rectangular apertures were taken as the detector centers. The size sensitivity was varied over a factor of six by changing the receiver lens masking from 12.7mm centroid spacing to 76.2mm centroid spacing. Except for some variation in the signal amplitude due to changes in receiver lens f/number, no changes other than receiver masking were necessary to vary the size sensitivity. Representative results of this testing using the monodisperse droplet generator are given in figures 25 thru 28. Receiver masking geometry is shown overlayed on each data listing with the centroid spacing specified under the parameter 'SLIT SEPARATION'. Measured drop size agrees very well with Berglund-Liu drop size ('B-L SIZE') in all cases.

It was assumed that the centroid of the masked area was the appropriate choice for detector location. To test this assumption, several masks were designed with similar centroid spacings but dissimilar geometries. typical results from these tests are given in figures 29 thru 31. Again, mask geometries are overlayed on the data histograms. In each case the centroid separation was fixed at 50.8mm. Changes in lens aperture resulted in changes in signal amplitude which were corrected by detector gain adjustment when necessary.

Spray Nozzle and Atomizer Tests

This series of tests involved the measurement of polydisperse droplet spray fields produced by industrial spray nozzles using water. Although the signal processor and data acquisition system lacked much of the sophistication necessary to make accurate measurement in this type of flow, the data obtained show remarkably good agreement with other measurement sources. In particular, signal rejection based on Doppler frequency and signal amplification over a dynamic size range greater than 35 were not available with the breadboard system. Nor was the third detector required for additional signal validation and ambiguity available.

The majority of the spray testing utilized spray nozzles from the Delavan Inc with flow capacities ranging from .5 to 1.0 GPH. Typical results for two different flowrate nozzles at 60 psig are shown in figures 32 and 33. These particular spray conditions were selected because of comparative drop size distribution information provided by Delavan[14]. Figures 34 and 35 show the phase Doppler measurements overlayed with the Delavan data.

Several other spray sources were used including garden variety nozzles and hand or finger operated pump bottles. Results from these tests were not included as no corroborating data was available.

A spinning disc atomizer was used to test the small drop size sensitivity of the instrument. A typical distribution is shown in figure 36. As expected the size distribution produced by the atomizer was very narrow with the majority of drops less than 40 micrometers diameter. The distribution of figure 36 can be compared to those of figures 37 and 38 in which the size sensitivity of the instrument was varied in an attempt to shift the location of the measured phase information. The self-consistency of these measurements can be seen when they are overlayed with normalized ordinates as in figure 39. The data presented in these tests is in the 'raw' form with no probe volume corrections even though this type of correction is believed to be necessary at the small size end of a given size range.

The atomizer used in the above tests produces a spray field of moderately high droplet number density. Simultaneous droplet probe crossings (multiple events) were observed from time to time on the oscilloscope. Although this path was not pursued, the system response to multiple events does not appear to preclude its use in high droplet number density environments.

Backscatter

In many applications, access to a spray field under test can be obtained from only one side of the test rig. At other times it is desirable to locate transmitter and receiver packages next to each other to provide system rigidity. In some situations the droplets themselves may be opaque to visible light (e.g. liquid metals) such that refractive scatter does not exist. In all of the above cases, the measurement of backscattered light could be utilized. The backscatter configuration involves arrangement of transmitter and receiver

such that light scattered back toward the source ($\theta = 150°$ in this case) is collected and analyzed. For the situation involving opaque drops, this light would be scattered by first surface reflections. For non-opaque drops, backscatter may also involve light scattered from secondary internal reflections which complicate the analysis.

Calculations of relative scatter intensities were performed prior to experimentation. The results showed that the light scattering intensity from the droplet surface (first surface reflection) of pure water drops was actually less than the light scattering intensity from light refracted into and internally reflected out of the droplets in the same backscatter direction. It was believed that if the relative intensities of light scattered between the two modes were sufficiently different, only the dominant mode should be detected. To support this assumption, phase shift calculations for the internal reflection mode ($\theta = 150°$) were completed and found to be nearly identical to the forward scatter refraction mode ($\theta = 30°$).

A water based dye was used during these experiments to vary the opacity of the droplets and suppress the internal reflective scatter by absorption of the incident light. Pure dye used to form droplets eliminated all internal reflections allowing only first surface reflection. Results involving pure dye are shown in figure 40 to accurately follow the prediction for first surface backscatter. Results using pure water and the prediction for internal reflection at $\theta = 150°$ are shown in figure 41. When the droplet opacity reached a certain value the results fell between the two extremes of figure 40 (essentially 100% opaque) and figure 41 (nearly transparent) and often contained data from both modes.

3.3 Signal Quality Effects

Several sources of possible signal degradation were investigated to observe their effect on the phase measurement scheme. These sources were identified by the investigators based on previous experience with similar light scatter instrumentation. The two categories into which these possible sources fall are optical alignment and incident beam interference. The probe volume of the phase measurement method is physically limited by the beam intersection region and the receiver pinhole. Only light which enters the pinhole will reach the detectors and this light must originate from the beam overlap region. This critical

alignment between transmitter and receiver can be affected in ways which could possibly produce deleterious effects on the size measurements. Perhaps even more crucial to signal phase measurements is the quality of the incident beams which form the probe volume. Incident beam quality directly affects the quality of the interference fringes. Beam drop-out or selective attenuation can alter fringe formation and contrast. The phase measurement technique was promoted because it was potentially less sensitive to loss of signal quality than existing instrumentation.

Alignment

During these evaluations, light gathered by the receiver lens was brought to a focus and passed through a pinhole spatial filter whose size was selected to match the beam waist at the probe volume. The purpose of the pinhole is two-fold: first, it prevents light from other sources (other parts of laser beams or background light) from reaching the detectors and second, it guarantees signal coincidence at both detectors. Pinhole misalignment can result in 'receiver aperturing' which alters the character of the detector signals. The monodisperse generator was especially useful when studying pinhole effects as its droplet stream could be directed through select parts of the laser beams effectively scattering light from a single 'point'. When first applied in the receiver package, tests were conducted to verify that the pinhole did not adversely affect the drop size measurement. The results of one such test is shown in figures 42 thru 45. A range of pinhole sizes was used including the smallest which was not expected to transmit all of the focussed light. No appreciable shift in measured size could be detected although the smallest pinhole produced a broadened distribution which may have been indicative of aperturing problems.

A second series of tests were run to observe induced aperturing effects on size measurements. These tests involved intentional focussing errors at the pinhole plane. Due to the nature of the focussed light, selective aperturing of light intended for individual detectors could occur. This aperturing led to signal distortions with the potential for errors and were, in fact, processed as erroneous drop sizes. A set of data from one such test is given in figures 46 thru 48. The errors induced in these tests were much more severe than those expected in practice.

The effect of receiver alignment on other than the center of the probe volume was investigated. At the extremes of the probe volume, a hyperbolic spreading of the interference fringes may take place. The monodisperse droplet stream was centered on the beam crossover and then moved to the detectable extremes of the crossover region. The receiver pinhole was removed for these tests. Figures 49 thru 54 show the data from these tests. A combination of loss of signal intensity and signal distortion determined the detectability limits. No appreciable change in droplet size was observed, although broadening of the distributions did occur and was attributed to the decrease in signal-to-noise ratio.

Beam Quality

Fringe contrast at the measurement probe volume is dependent upon relative beam intensity, beam polarization and coherence. Loss of fringe contrast is disastrous for sizing techniques based on signal visibility since this quantity is directly related to the fringe contrast or visibility. Although fringe contrast is easily affected, fringe spacing is not. The phase technique is directly dependent upon fringe spacing but not upon fringe visibility and thus, should not suffer from losses of contrast. To verify this, tests were conducted in which the fringe visibility was intentionally lowered. The monodisperse generator was used as the droplet source. Figure 55 shows results for the case of 100% fringe contrast in which incident beam intensities were nearly equal. A neutral density filter of optical density 1.0 was then inserted into one of the two beams changing the intensity ratio from 50:50 to 91:9 and reducing fringe visibility to only 20%. The test was repeated with the results given in figure 56. The size measurement was not affected.

Losses of beam intensity and fringe visibility do not occur as cleanly as was suggested by the previous testing. In a spray environment, droplets pass randomly through the incident beams scattering light away from the incident direction, affecting both beam intensity and coherence. Droplets with sizes comparable to that of the beam diameter can cause beam drop-out. The combined effect of many small droplets in the incident beams can result in a severe decrease in signal-to-noise ratio. The oscilloscope trace of figure 57 shows a typical beam attenuation due to droplet interference. Since each of the two incident beams is affected similarly, but not identically, by droplet passage, the character of the beams which intersect at the probe volume at any instant cannot be easily predicted.

Spray interference effects on droplet measurements was investigated by introducing a spray into the path of the incident beams while measuring the monodisperse droplet stream. Since droplet size to beam diameter is an important parameter in this test, two spray droplet distributions of widely differing mean drop sizes were used. Spray interference will also affect light scattered from the probe to the receiver lens. This interference, however, is not as severe as beam drop-out. The results of a spray interference test is given in figures 58 thru 60. In each case the interfering spray was judged to contain a moderate to high droplet number density. Test results show that mean size measurements did not change although some broadening of the distribution did occur and is attributed to loss of signal-to-noise ratio and spray interference directly with the monodisperse droplet stream.

4.0 SUMMARY AND CONCLUSIONS

An innovative approach for spray drop size and velocity characterizations has been described. The method, which obtains the drop size information from the interference fringe pattern produced by the scattered light, has been shown to have several advantages. Perhaps the most significant advantage is the relative insensitivity of the method to uncertainties in the scattered light intensity and fringe visibility which occur when the laser beams are attenuated by the droplets or other optical contamination. The linear relationship between the measured signal phase and the dimensionless drop size simplifies the implementation of the method and creates a uniform size sensitivity over the measurement range. The dynamic size range of the technique is essentially limited only by the dynamic range of the detectors and the prevailing signal-to-noise ratio.

Monodisperse droplet streams were used as a basic test of the theory and to test susceptibility of the method to practical effects experienced in the application of the method. These effects included optical imperfections, environmental conditions and simple alignment errors. In terms of the operating requirements and errors produced, the operation was analogous to the conventional laser Doppler velocimeter.

Methods for size range selection were described and tested. Either the beam intersection angle (fringe spacing) or the detector spacing can be changed to achieve the same result. The detector or slit spacing was easy to implement, did not require realignment and did not change the Doppler difference frequency. Also, this method has only a minimal effect on the probe volume.

Sprays were measured in this preliminary assessment of the technique. Comparisons of the measurements to other methods were presented and the results showed reasonably good agreement. However, this cannot be used to make conclusions about the relative measurement accuracy. Measurements at different size range selections were also made to determine the self-consistency of the method. The availability of a "standard spray" would facilitate the evaluation of these new diagnostic techniques.

Although the tests conducted using the breadboard processor were as extensive as possible, further tests are required using the more advanced prototype processor currently

under development. The processor will produce two simultaneous phase measurements to prevent ambiguity and to reject spurious signals that may occasionally pass the noise rejection logic. Testing of the processor's automatic setup functions and signal qualification logic will be the first priority in the future work. The processor will be capable of a data rate greater than 10,000 samples per second so that tests on the probe volume effects and mass flowrate determinations can be considered.

In summary, the recognized potential characteristics of the method are:

- linear relationship between the measured phase angle and drop size
- size range of 30 or greater at a single optical setting
- overall size range of 3 to 2000 microns
- simultaneous size and velocity measurements
- relative insensitivity to beam or light scatter attenuation
- high spatial resolution
- operation is similar to an LDV
- adaptable to existing LDV systems
- can distinguish between gas phase and droplets
- reduced sensitivity to misalignment
- can perform measurements independent of refractive index.

A patent application has been filed.

REFERENCES

1. A. M. Taweel, and J. Landau, "Turbulence Modulation in Two-Phase Jets," *Journal of Multiphase Flow*,Vol 3, 1977, pp. 341-351.
2. W. H. Snyder, and J. L. Lumley, "Some Measurements of Particle Velocity Autocorrelation Functions in a Turbulent Flow," *Journal of Fluid Mechanics*,Vol. 48, 1971
3. V. Goldschmidt, and S. Eskinazi, "Two-Phase Turbulent Flow in a Plane Jet," *Journal of Applied Mechanics*,Vol. 33, Ser. 3, No. 4, 1966.
4. D. Modarress, J. Wuerer, and S. Elghobashi, "An Experimental Study of a Turbulent Round Two-Phase Jet," St. Louis, Missouri, AIAA Paper No. 82-0964, June 1982.
5. R. A. Dobbins, L. Crocco, and I. Glassman, "Measurement of Mean Particle Sizes of Sprays From Diffractively Scattered Light," *Am. Inst. Aeronaut. Astronaut. J.* Vol. 1, p. 1882.
6. J. Swithenbank, J. M. Beer, D. S. Taylor, D. Abbott, and G. C. McCreath, "A laser Diagnostic for the Measurement of Droplet and Particle Size Distribution," AIAA 14th Aerospace Sciences Meting, Washington, D. C., Paper No. 76-79, Jan. 1977.
7. W. M. Farmer, "Measurement of Particle Size, Number Density, and Velocity Using a Laser Interferometer," *Appl. Opt.,rm Vol. 11, 1972, p. 2603.*
8. *A. J. Yule, N. A. Chigier, S. Atakan, and A. Ungut, "Particle Size and Velocity Measurement by Laser Anemometry," AIAA 15th Aerospace Sciences Meeting. Los Angeles, Paper no. 77-214, 1977.*
9. *W. D. Bachalo, "Method for Measuring the Size and Velocity of Spheres by Dual-Beam Light-Scatter Interferometry," Appl. Opt.,"* Vol. 19, No. 3, 1980.
10. H. C. van de Hulst, Light Scattering by Small Particles, Wiley, New York, 1957.
11. J. R. Hodkinson and I. Greenleaves, "Computations of Light-Scattering and Extinction by Spheres According to Diffraction and Geometrical Optics, and Some Comparisons with the Mie Theory," *Journal of the Optical Society of America*,Vol. 53, No. 5, 1963. p. 577.
12. W. J. Glanschnig and S. Chen, "Light Scattering From Water Droplets in the Geometrical Optics Approximation," *Applied Optics,"* Vol. 20, No. 14, 15 July, 1981.

13. Berglund-Liu Monodisperse Droplet Generator, Thermo Systems Inc., Minneapolis, Minn.

14. Correspondence with Dr. Roger Tate, Delavan Inc, West Des Moines, Iowa.

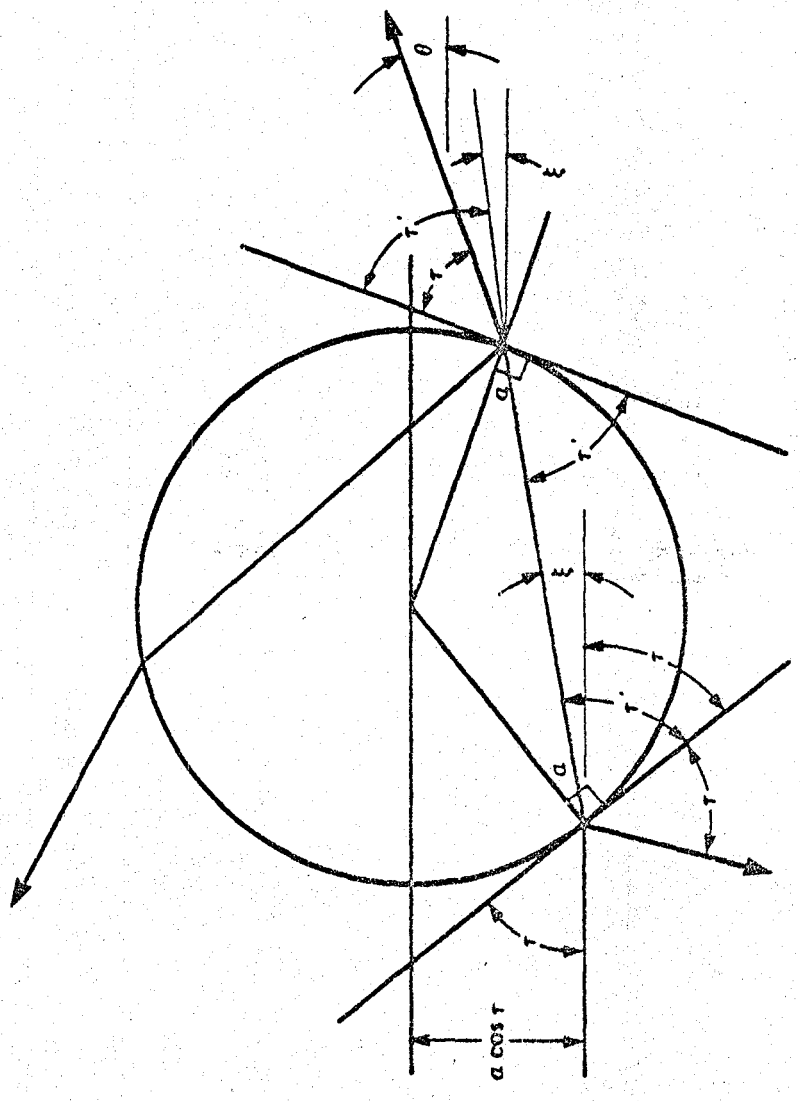

FIGURE 1. - Geometrical ray trace of an incident light ray through a sphere.

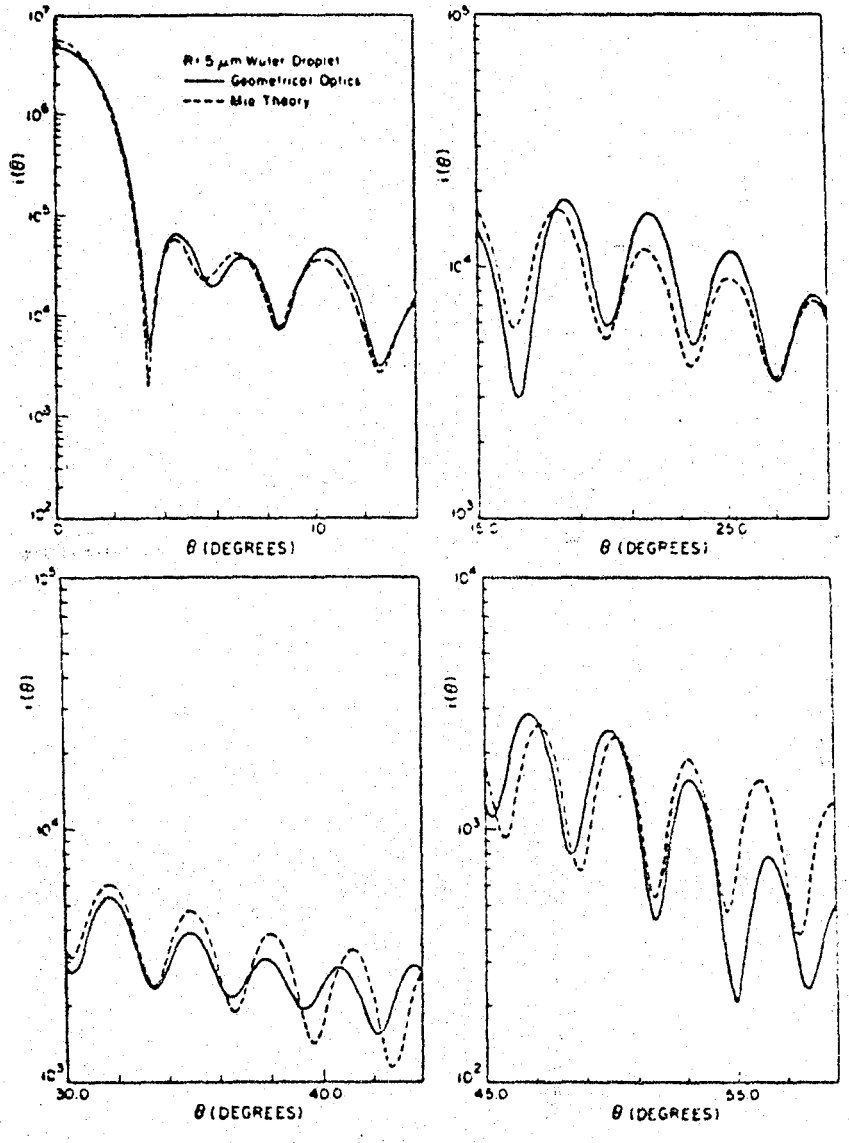

FIGURE 2. - Comparisons of angular scattering diagrams for 5 micrometer droplets computed from geometrical optics and Mie approaches.

FIGURE 3.- Schematic of the optical system for an LDV and droplet sizing system.

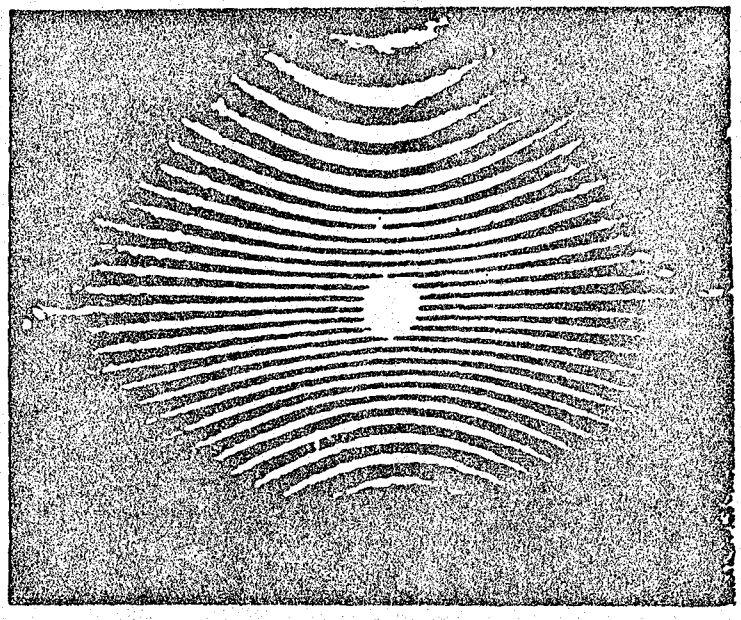

FIGURE 4. - Far field scattered light interference fringe pattern produced by a droplet.

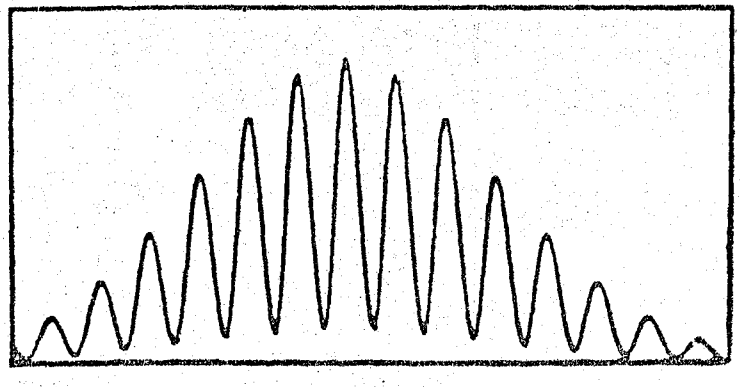

FIGURE 5. - Laser Doppler burst signal.

FIGURE 6.- Signal visibility versus dimensionless drop size; f/5 and collection angle = 30

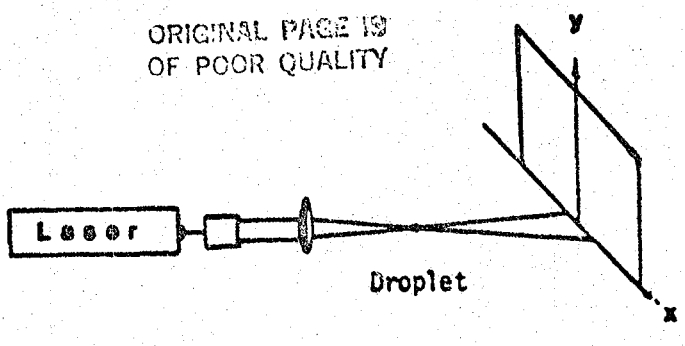

DROPLET DIAMETER=	160.0000
RECEIVER FOCAL LENGTH=	636.0000
DIAMETER RECEIVER =	125.0000
THETA =	0.0000
FRINGE SPACING =	50.0000
LASER WAVELENGTH =	.6328
INDEX OF REFACTION =	1.3300

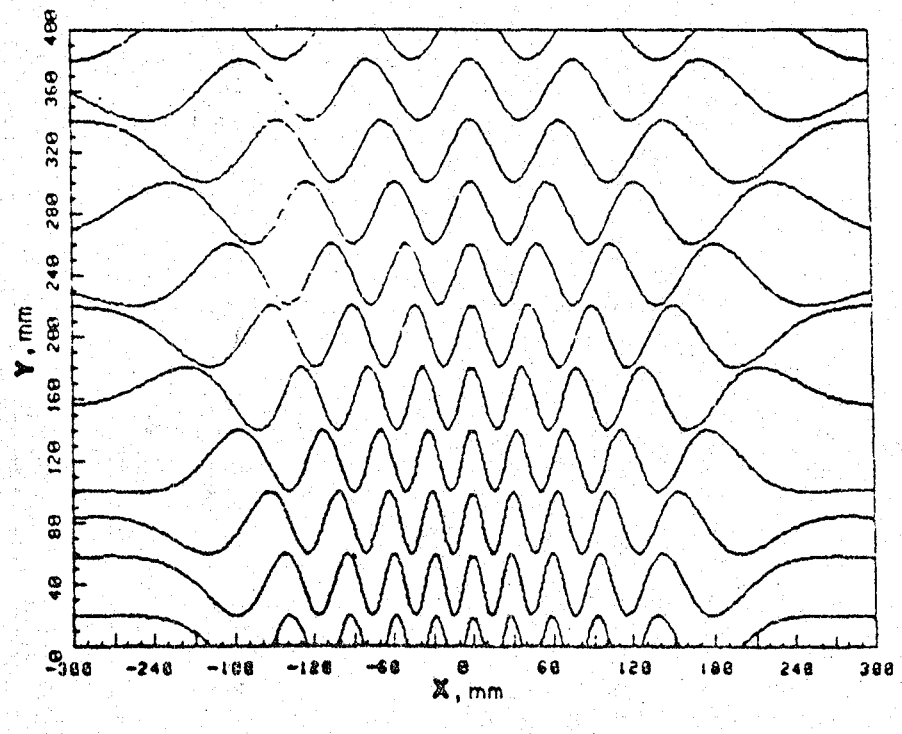

FIGURE 7.- Computed interference fringe pattern produced by a droplet

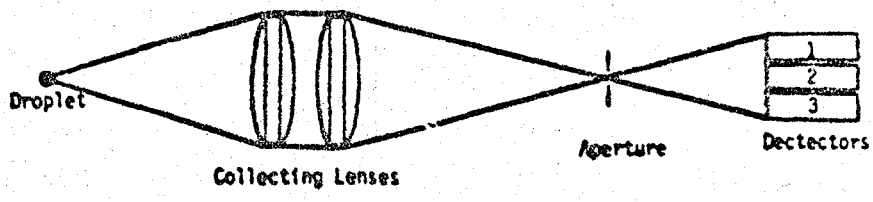

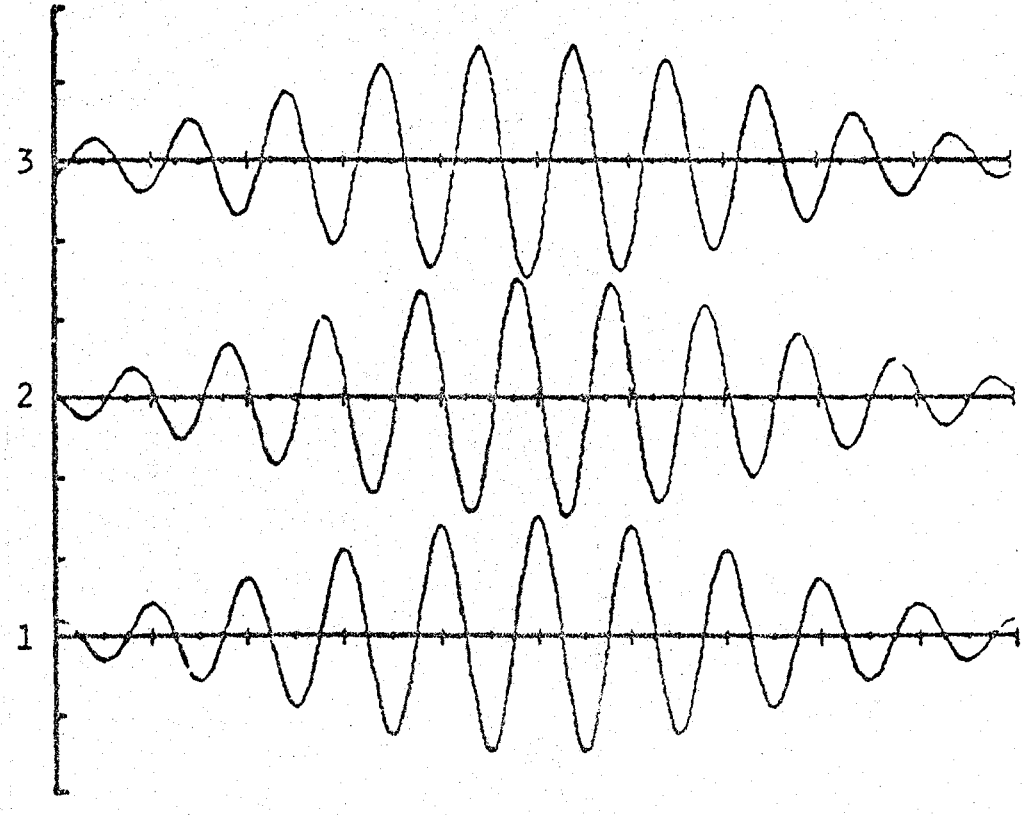

FIGURE 8. - Schematic of the detector arrangement and the resulting high pass filtered signals.

FIGURE 9.- Theoretical prediction showing the phase variation with the dimensionless drop size

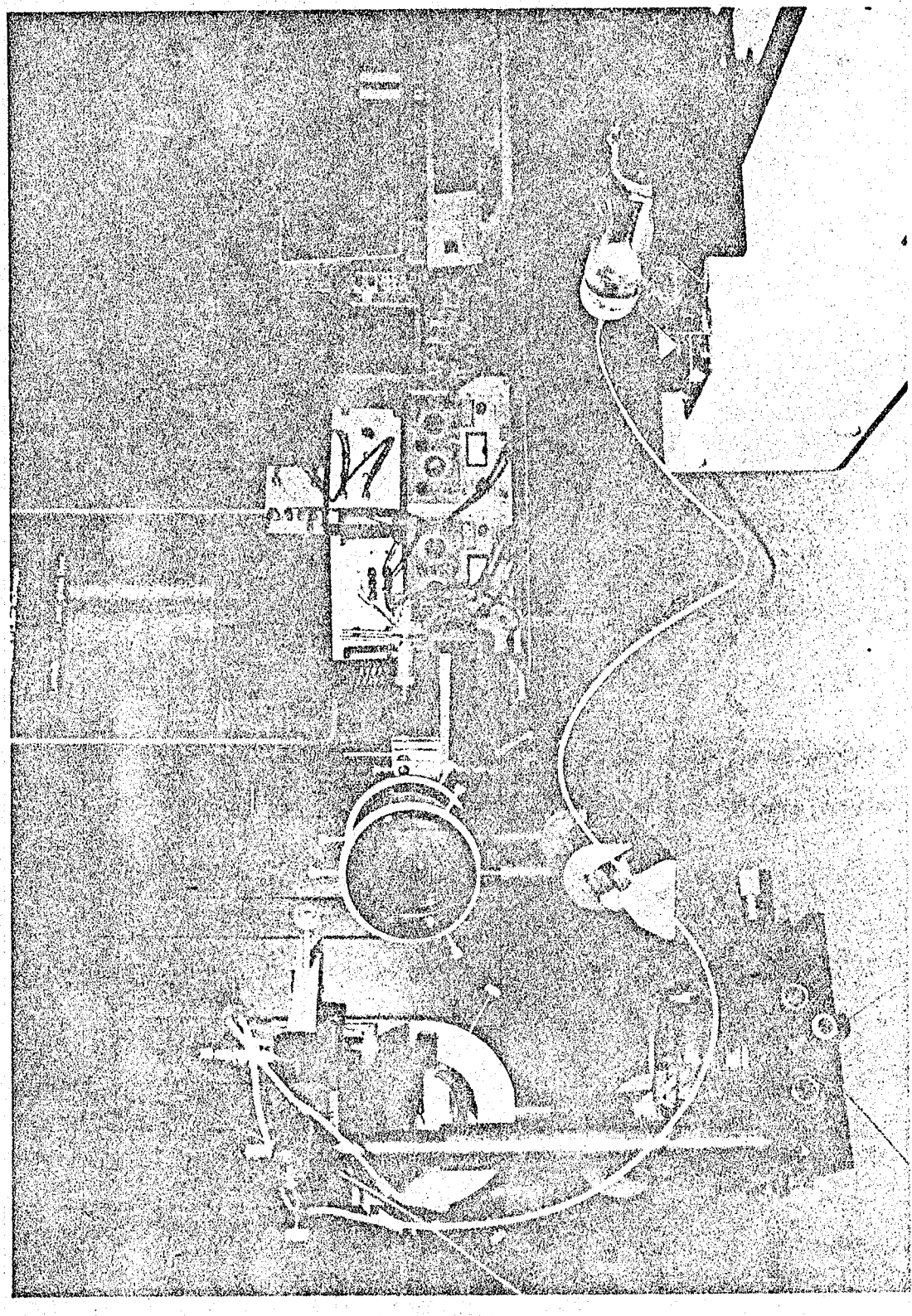

FIGURE 10 - Photograph of Phase/Doppler Instrumentation

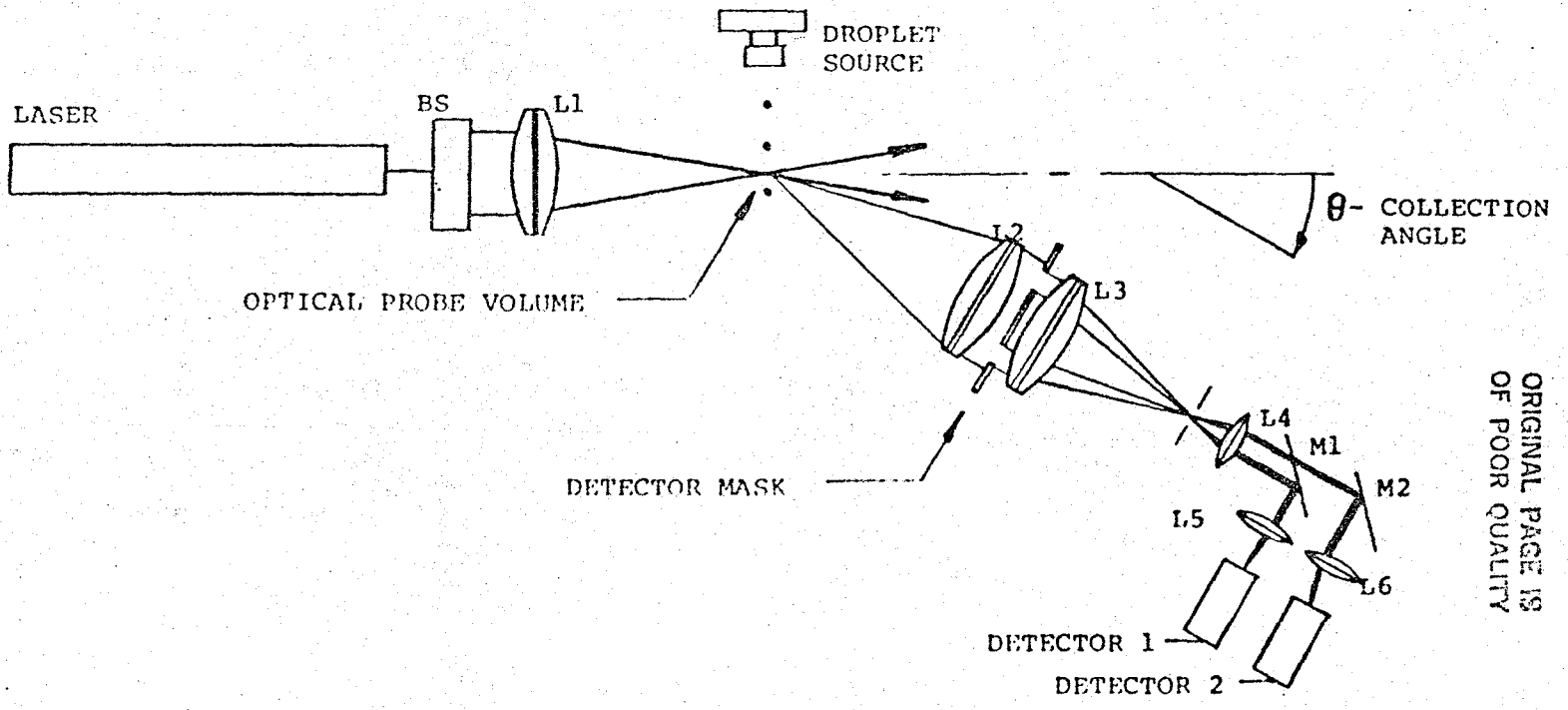

FIGURE 11 - Optical Component Layout

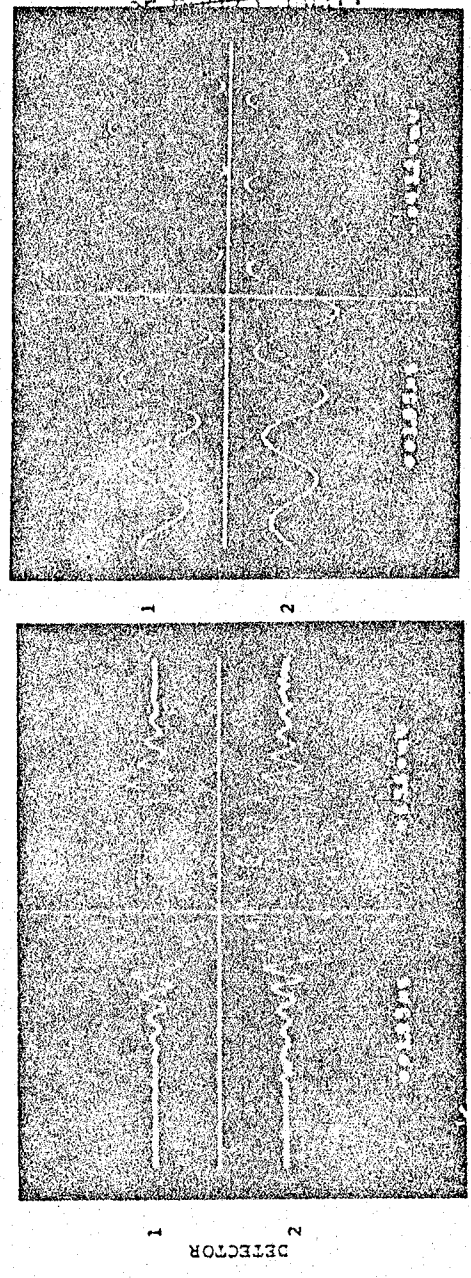

FIGURE 12 - Oscilloscope Traces Showing Signal Phase Shift

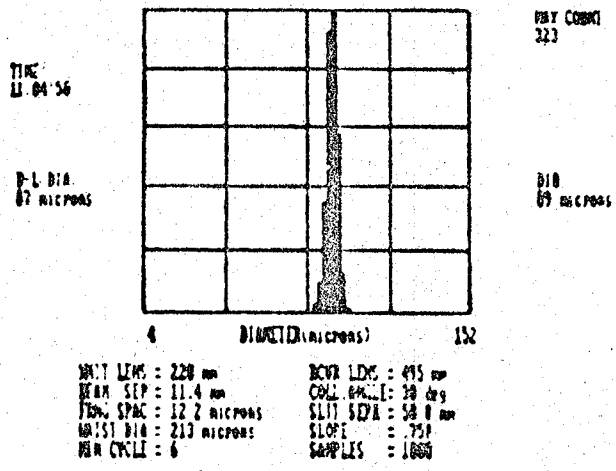

ORIGINAL PAGE IS
OF POOR QUALITY

Figure 13 - Drop size variations

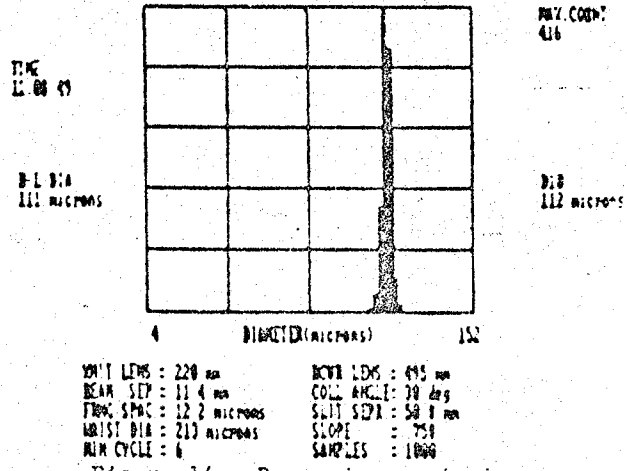

Figure 14 - Drop size variations

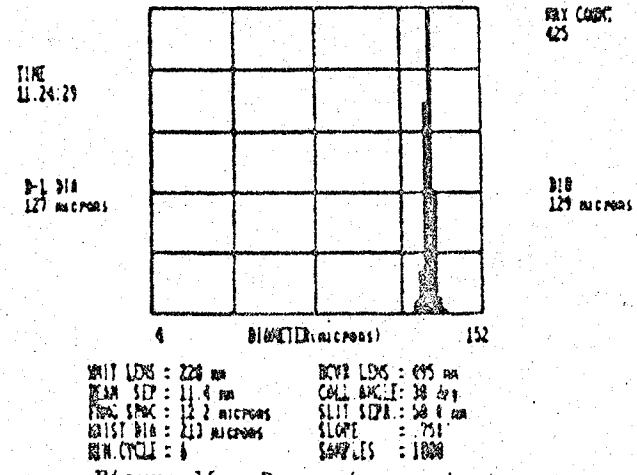

Figure 15 - Drop size variations

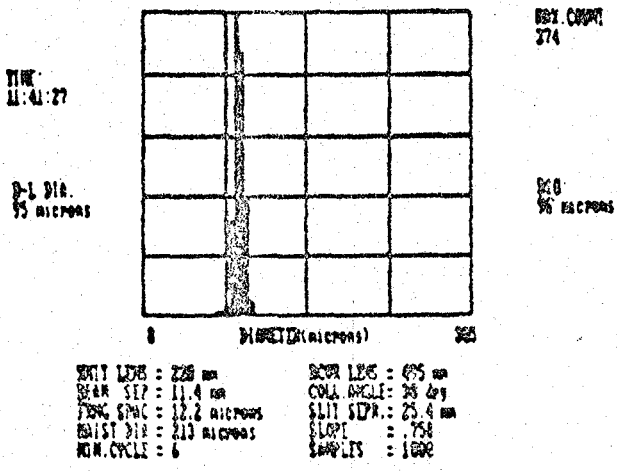

Figure 16 - Drop size variations

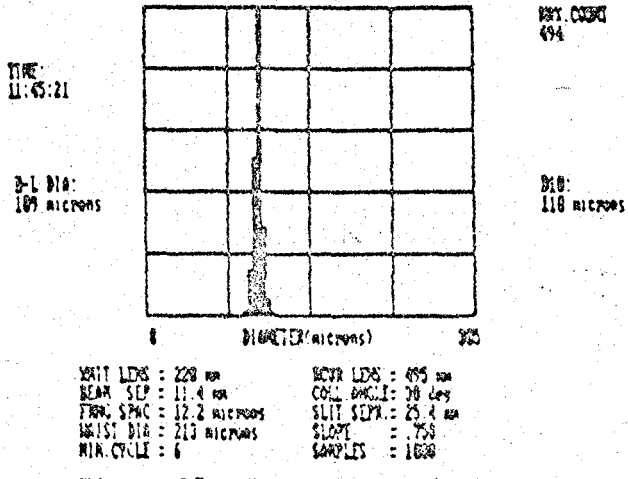

Figure 17 - Drop size variations

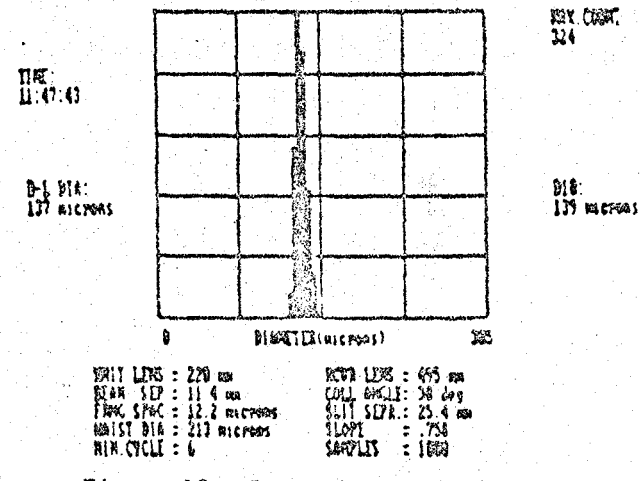

Figure 18 - Drop size variations

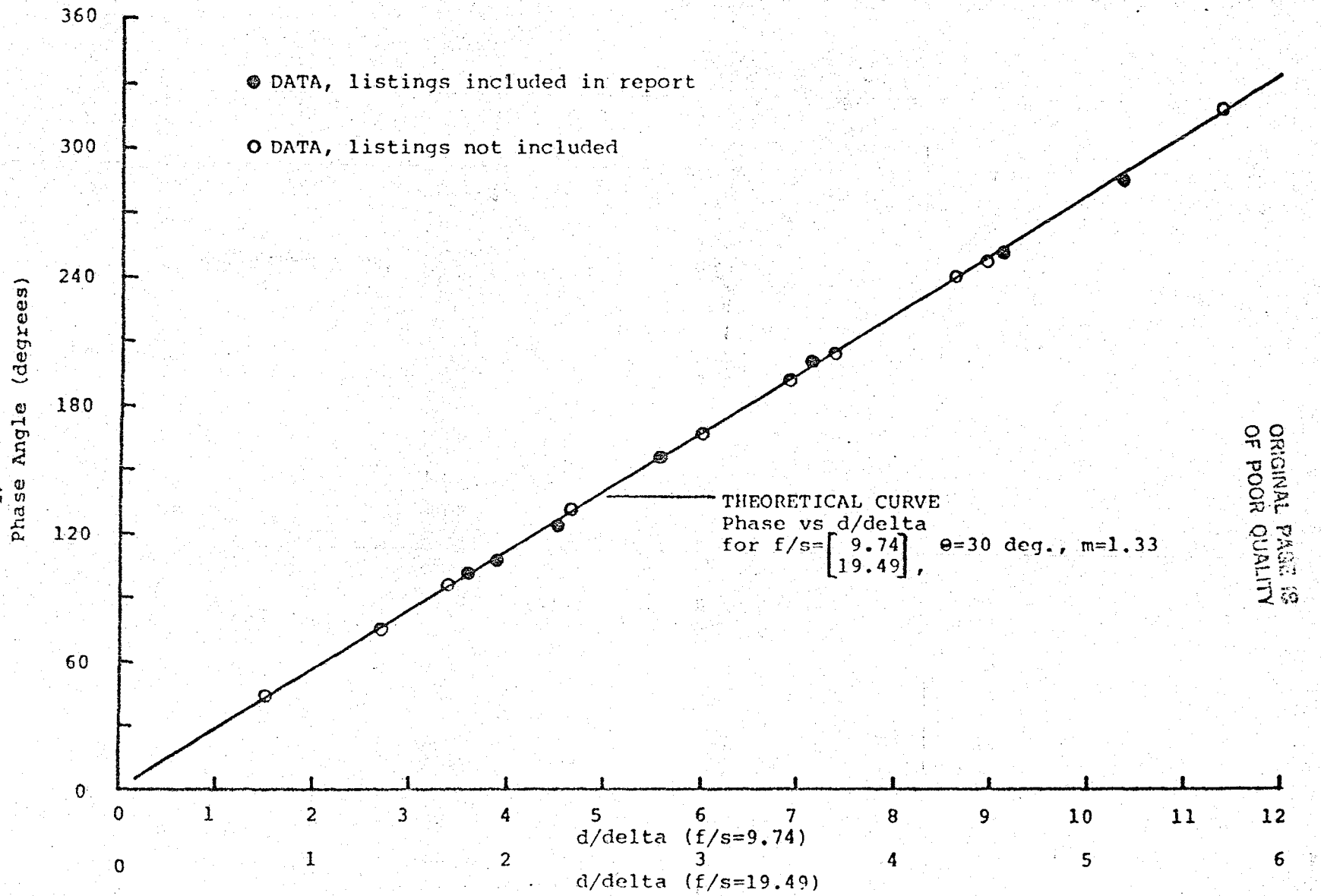

FIGURE 19 - Plot of Phase Shift vs Non-dimensional Size;
Theoretical Predictions and Experimental Data

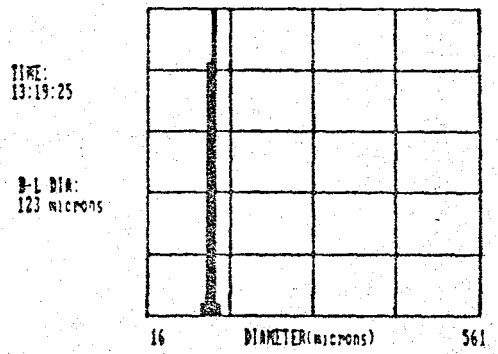

XMIT LENS : 220 mm
BEAM SEP : 3.1 mm
FRNG SPAC : 44.9 microns
WAIST DIA : 213 microns
MIN.CYCLE : 6

RCVR LENS : 495 mm
COLL.ANGLE: 20 deg
SLIT SEPR.: 50.8 mm
SLOPE : .758
SAMPLES : 1000

FIGURE 20 - Fringe Spacing Variations

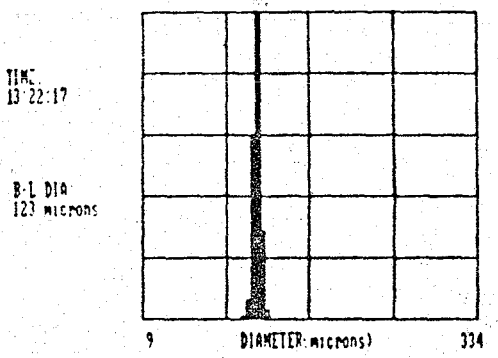

XMIT LENS : 220 mm
BEAM SEP : 5.2 mm
FRNG SPAC : 26.7 microns
WAIST DIA : 213 microns
MIN.CYCLE : 6

RCVR LENS : 495 mm
COLL ANGLE: 30 deg
SLIT SEPR.: 50.8 mm
SLOPE : .758
SAMPLES : 1000

FIGURE 21 - Fringe Spacing Variations

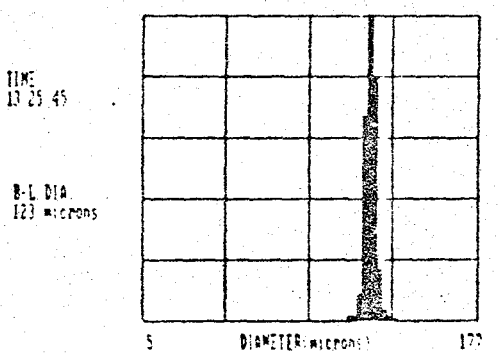

XMIT LENS : 220 mm
BEAM SEP : 9.8 mm
FRNG SPAC : 14.2 microns
WAIST DIA : 213 microns
MIN.CYCLE : 6

RCVR LENS : 495 mm
COLL ANGLE: 30 deg
SLIT SEPR : 50.8 mm
SLOPE : .758
SAMPLES : 1000

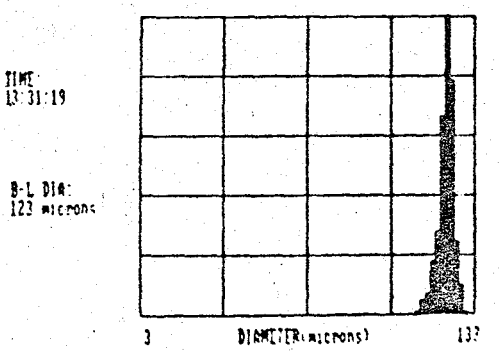

XMIT LENS : 220 mm
BEAM SEP : 13 mm
FRNG SPAC : 10.7 microns
WAIST DIA : 213 microns
MIN.CYCLE : 6

RCVR LENS : 495 mm
COLL ANGLE: 30 deg
SLIT SEPR : 50.8 mm
SLOPE : .758
SAMPLES : 1000

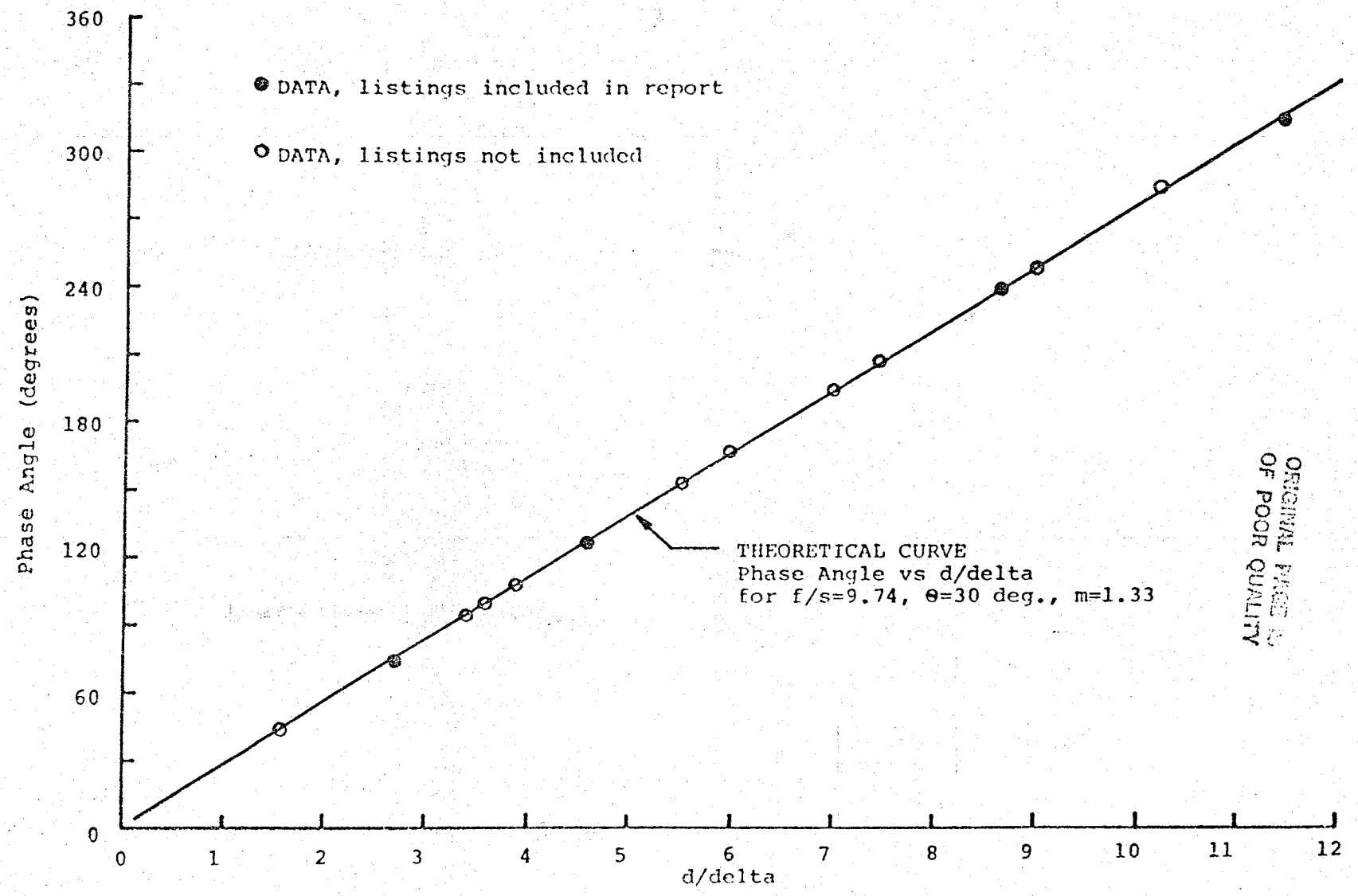

FIGURE 24 - Plot of Phase Shift vs Non-dimensional Size;
Theoretical Predictions and Experimental Data

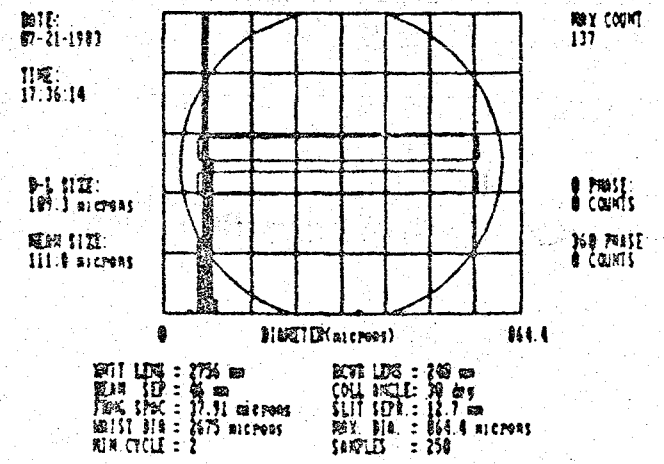

Figure 25 - Detector spacing variations;
S= 12.7 mm

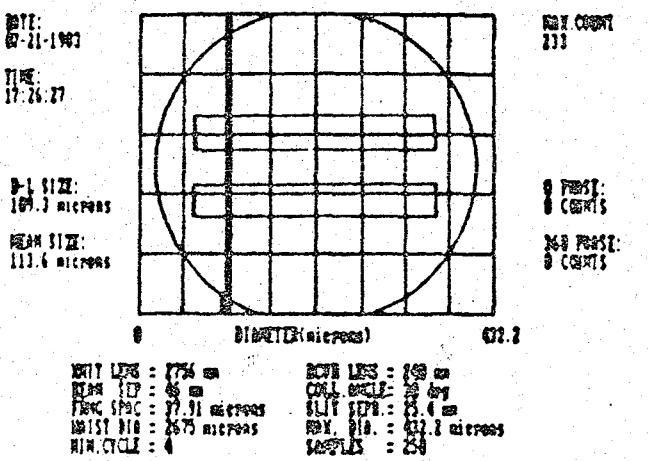

Figure 26 - Detector spacing variations;
S= 25.4 mm

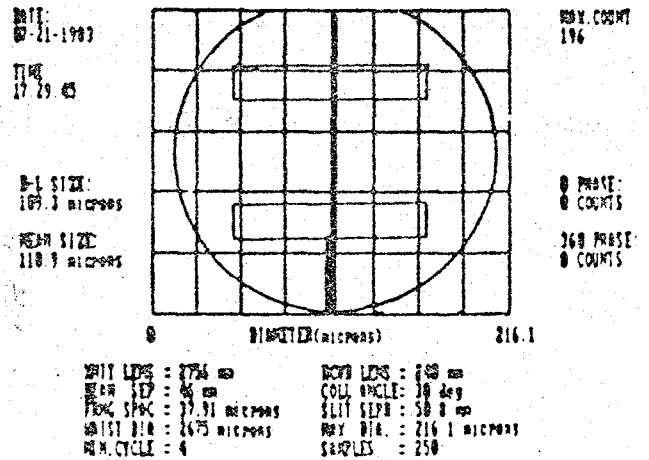

Figure 27 - Detector spacing variations;
S= 50.8 mm

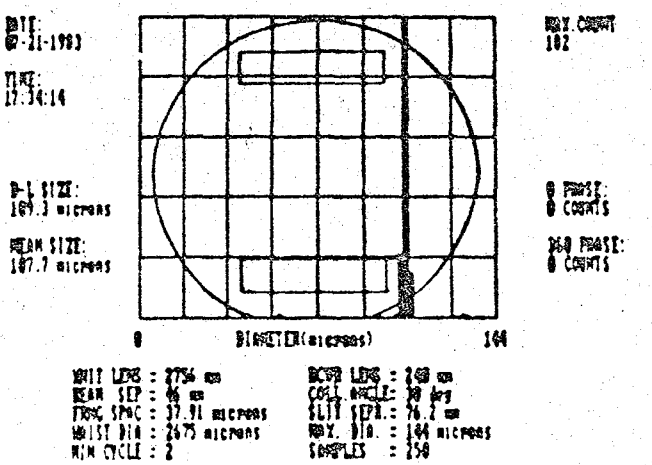

Figure 28 - Detector spacing variations;
S= 76.2 mm

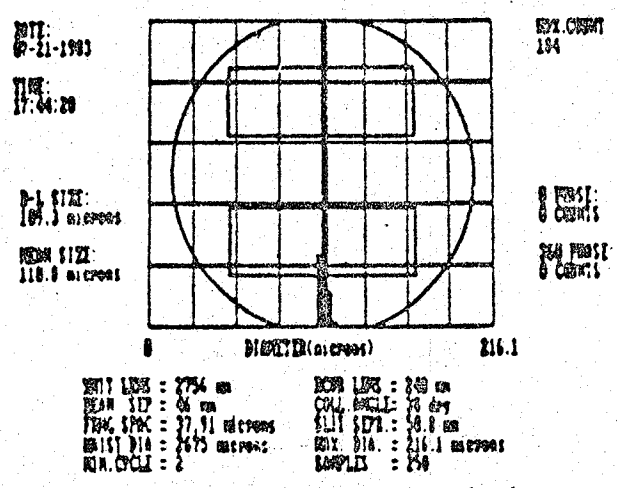

Figure 29 - Detector area variations

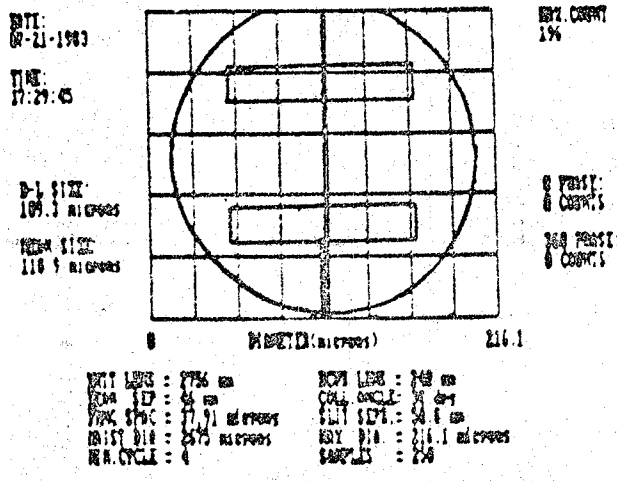

Figure 30 - Detector area variations

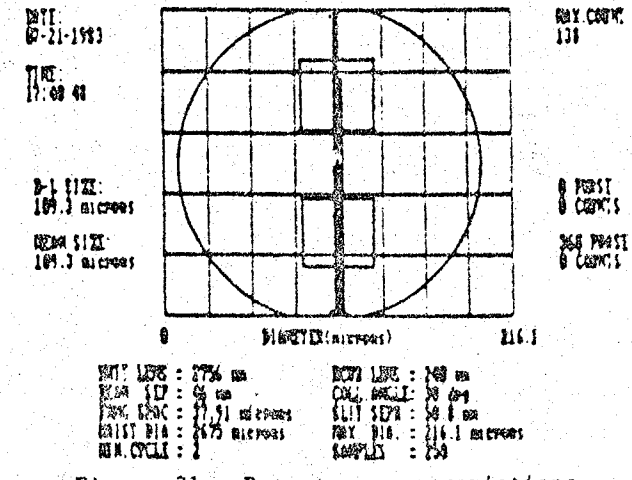

Figure 31 - Detector area variations

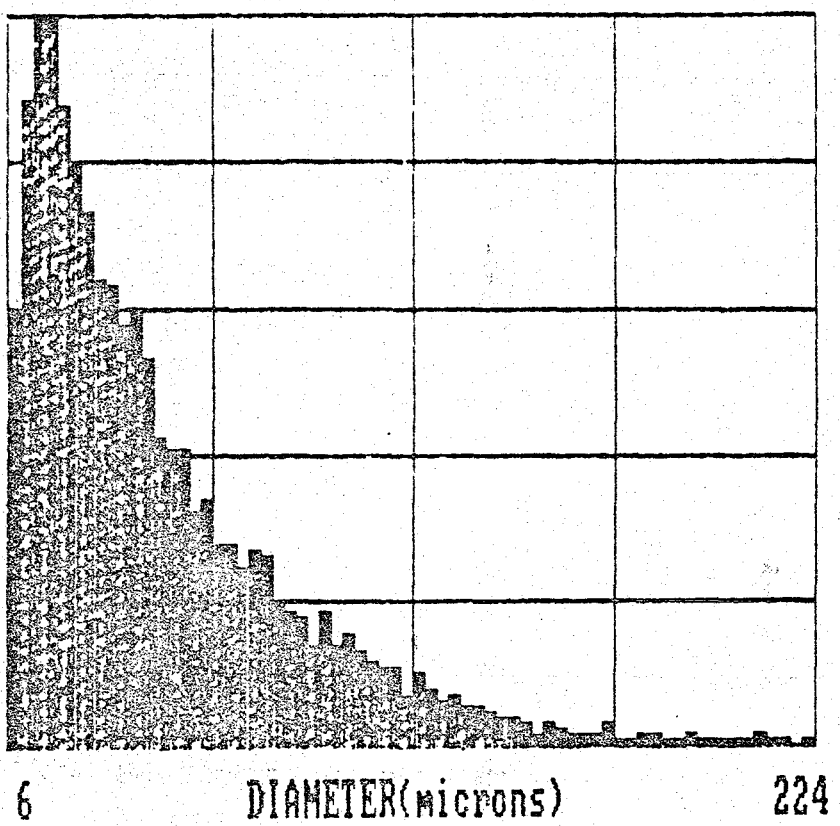

FIGURE 32 - Drop Size Distribution: Delavan 45B .6 GPH
60 psig Water, 10" below nozzle centerline

DATE:
10-19-1983

TIME:
17:19:24

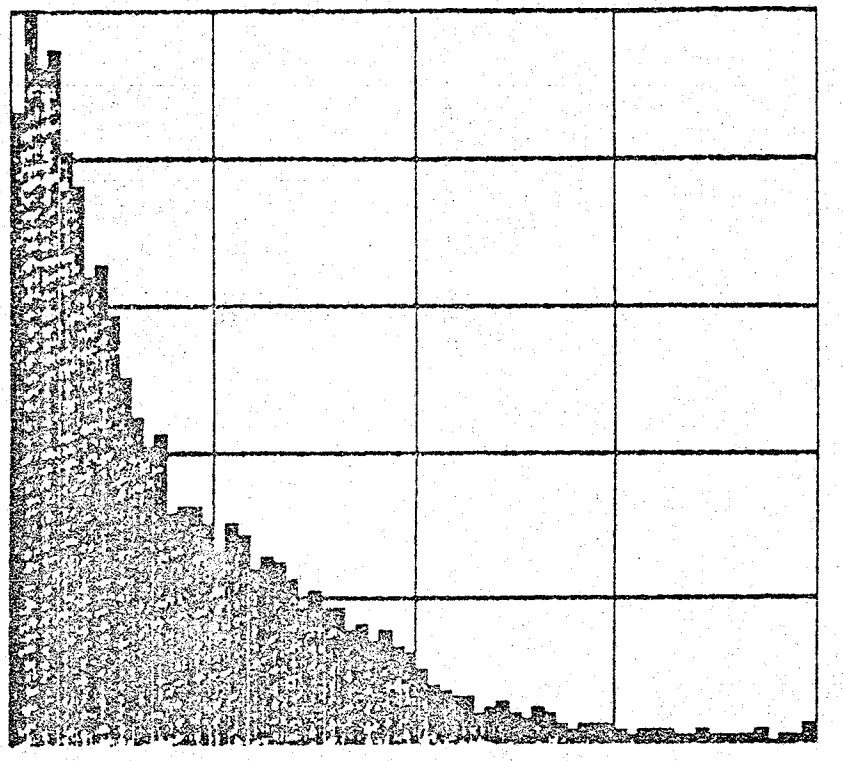

MAX.COUNT
685

MEAN SIZE:
48 microns

SMD:
108 microns

6 DIAMETER(microns) 224

XMIT LENS = 220 MM
BEAM SEP = 7.74 MM
FRNG SPAC = 17.9 microns
WAIST DIA = 213 microns
MIN.CYCLE = 3

RCVR LENS = 495 MM
COLL.ANGLE= 30 deg
SLIT SEPR.= 50.8 MM
SLOPE = .758
SAMPLES = 10000

FIGURE 33 - Drop Size Distribution: Delavan 45B 1.0 GPH
60 psig Water, 10" below nozzle centerline

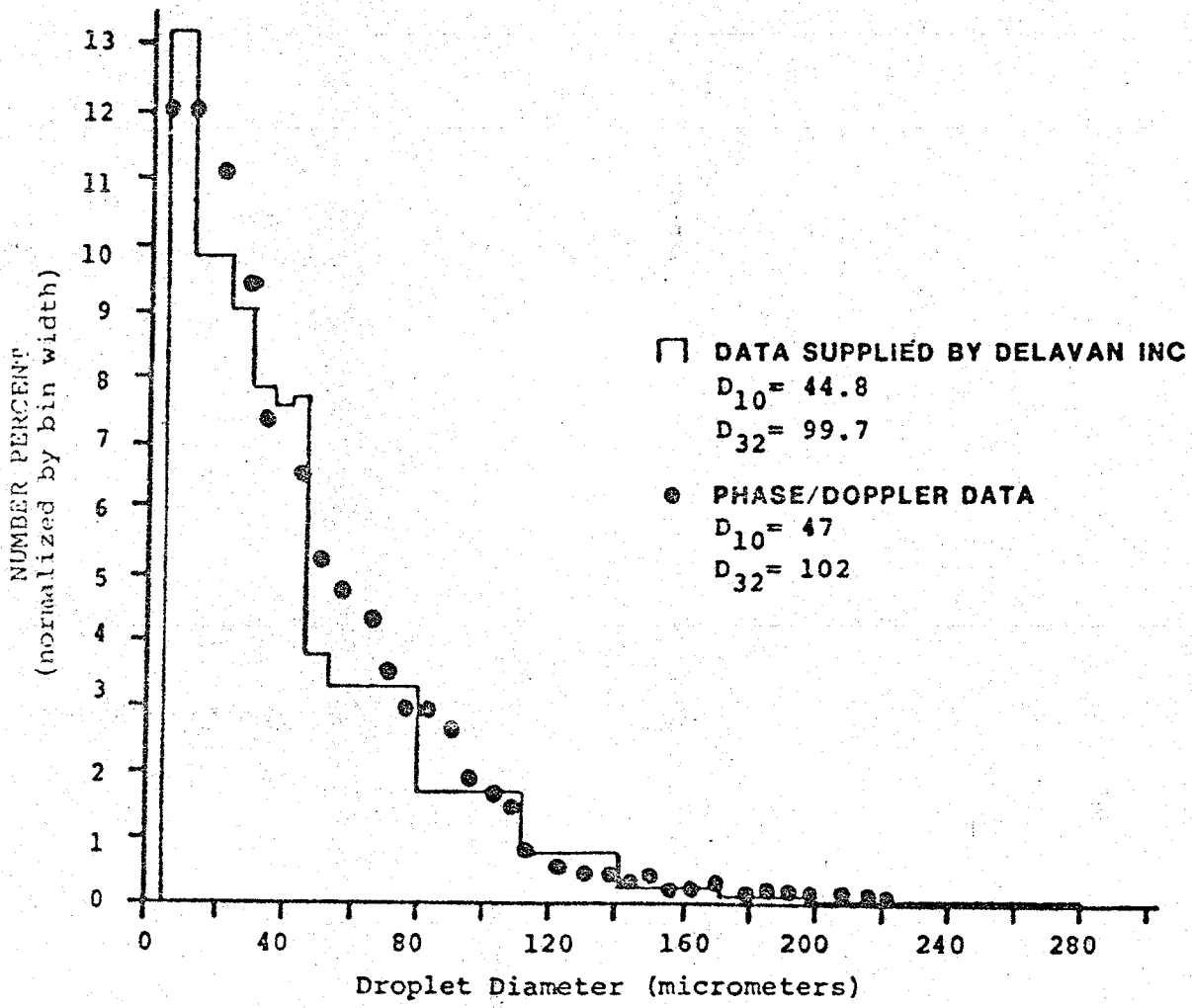

FIGURE 34 - Drop Size Distribution Overlays
Delavan 45B .6 GPH, 60 psig, 10" below CL

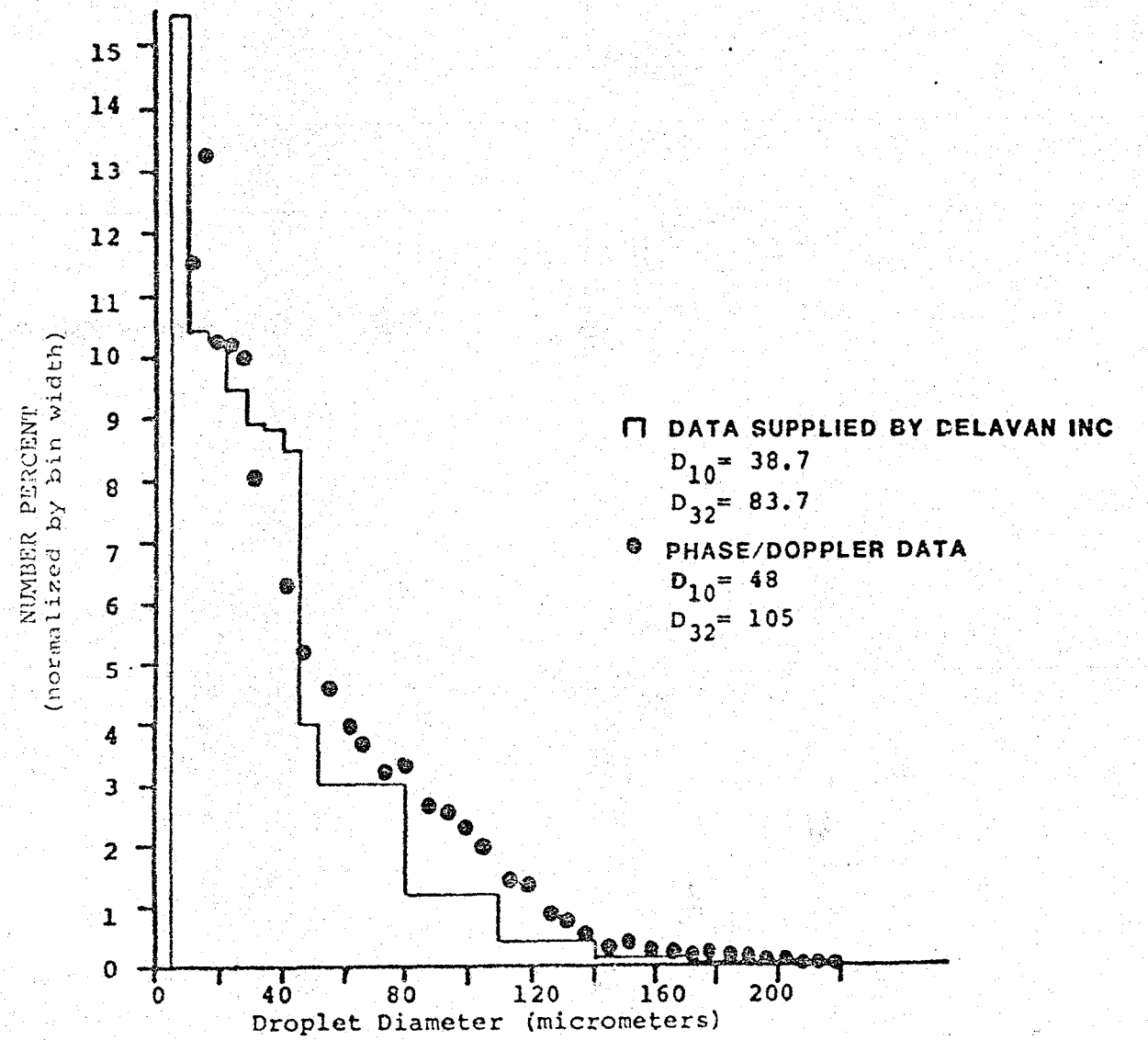

FIGURE 35 - Drop Size Distribution Overlays
Delavan 45B 1.0 GPH, 60 psig, 10" below CL

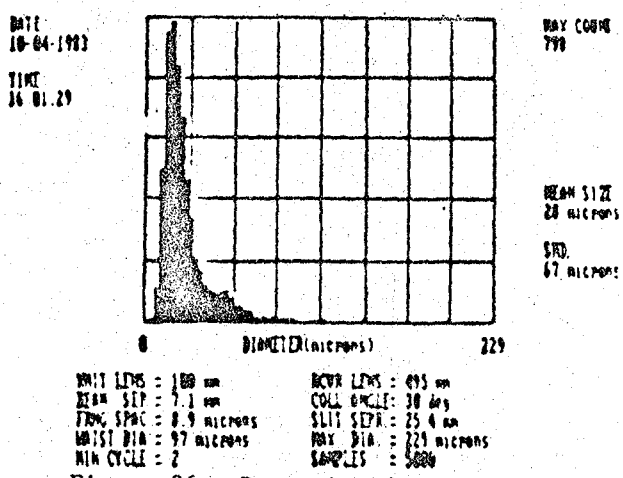

Figure 36 - Drop size distribution:
spinning disk atomizer
size range 229 micrometers maximum

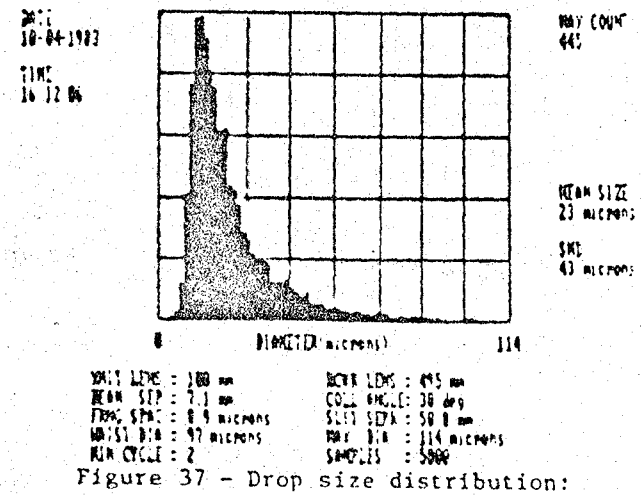

Figure 37 - Drop size distribution:
spinning disk atomizer
size range 114 micrometers maximum

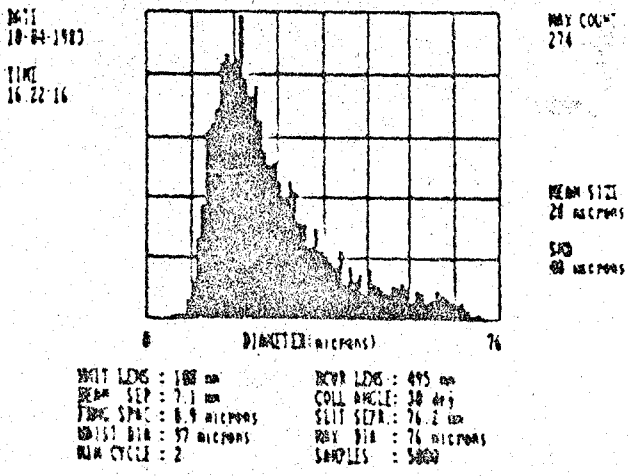

Figure 38 - Drop size distribution:
spinning disk atomizer
size range 76 micrometers maximum

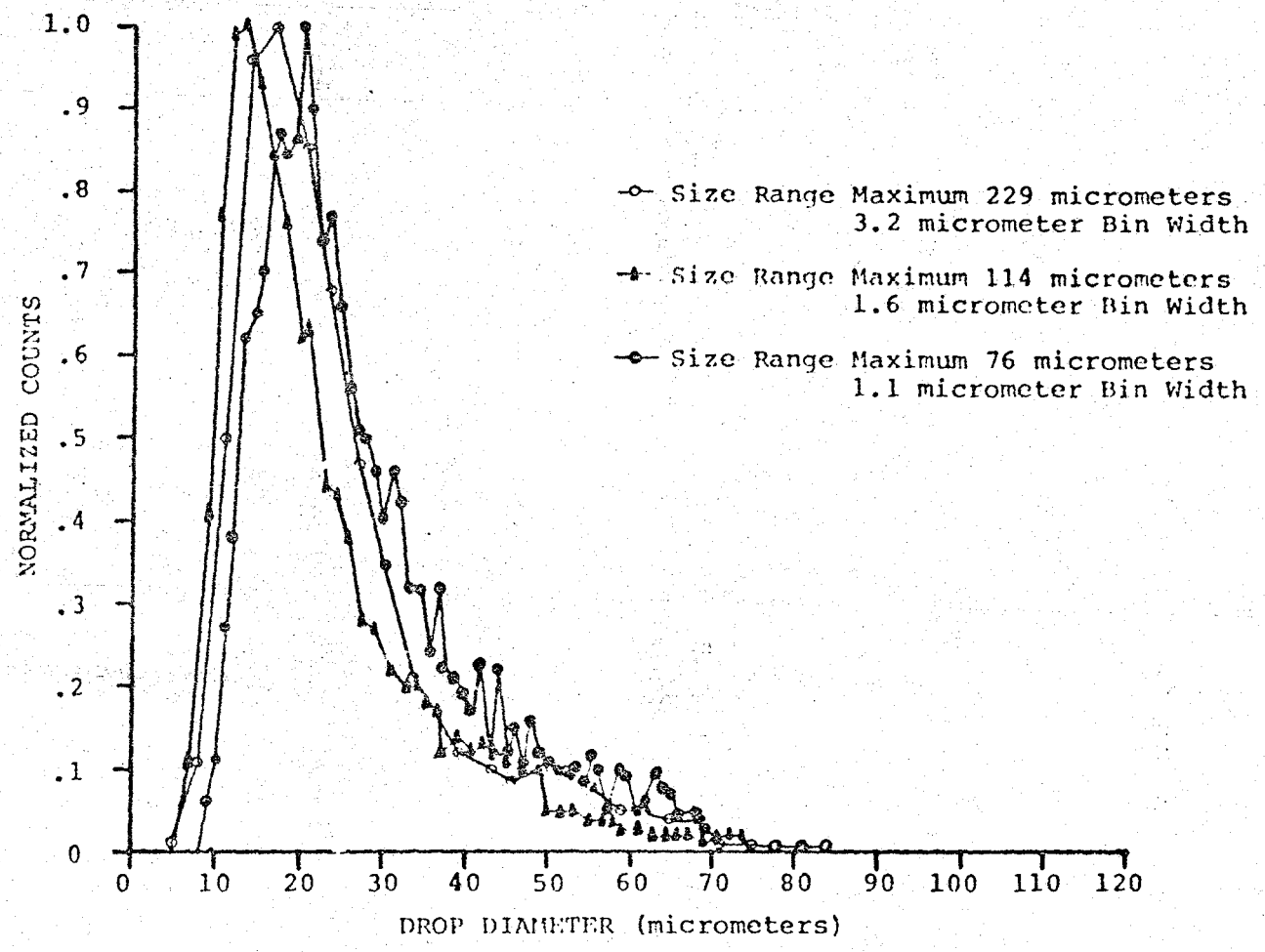

FIGURE 39 - Drop Size Distribution Overlays: Spinning Disk Atomizer

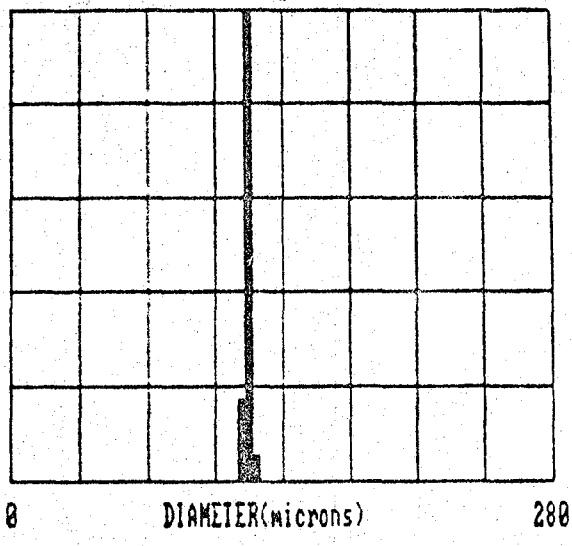

XMIT LENS = 220 mm
BEAM SEP = 18.6 mm
FRNG SPAC = 7.4 microns
WAIST DIA = 213 microns
MIN.CYCLE = 10

RCVR LENS = 495 mm
COLL.ANGLE= 150 deg
SLIT SEPR.= 50.8 mm
MAX. DIA. = 280 microns
SAMPLES = 8237

FIGURE 40 - Backscatter Test: 100% Dye (Opaque) Drops:
Using Prediction for First Surface Reflection

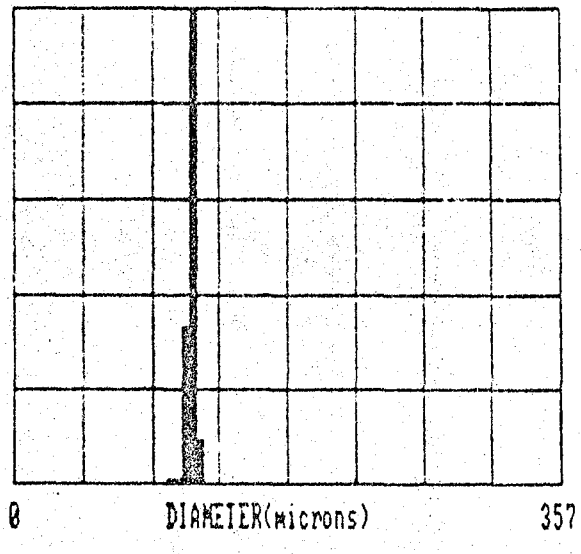

XMIT LENS = 220 mm
BEAM SEP = 5 mm
FRNG SPAC = 27.8 microns
WAIST DIA = 213 microns
MIN.CYCLE = 3

RCVR LENS = 495 mm
COLL.ANGLE= 150 deg
SLIT SEPR.= 50.8 mm
MAX. DIA. = 357 microns
SAMPLES = 1005

FIGURE 41 - Backscatter Test: Water (Nearly Transparent) Drops:
Using Prediction for Internal Reflection

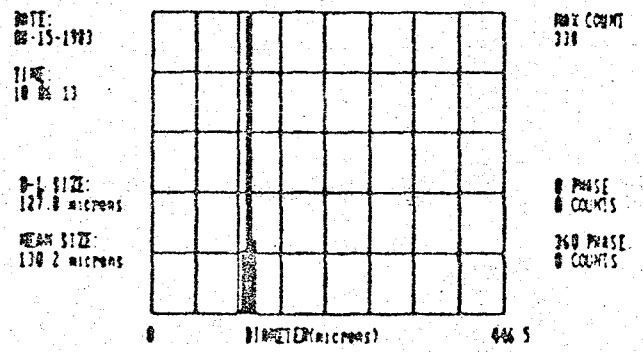

Figure 42 - Pinhole effect test: no pinhole, baseline data

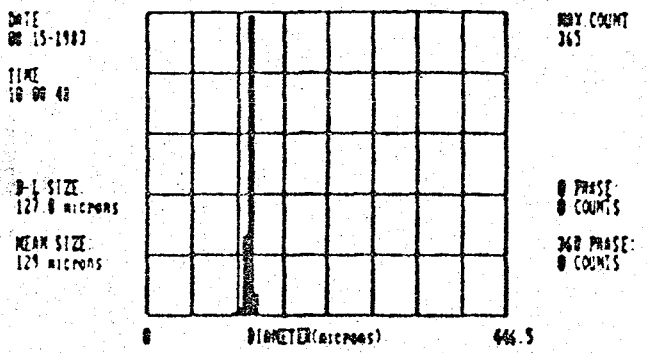

Figure 43 - Pinhole effect test: 800 micrometer pinhole

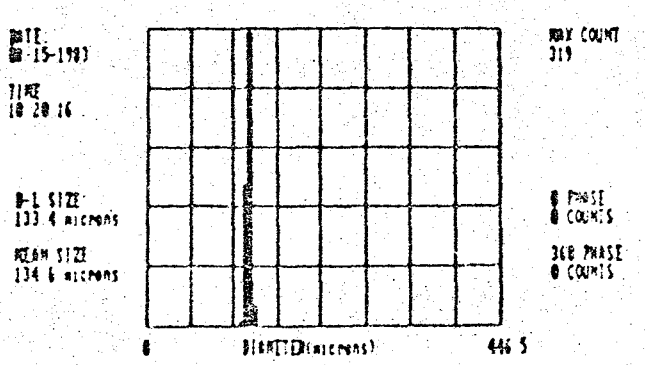

Figure 44 - Pinhole effect test: 400 micrometer pinhole

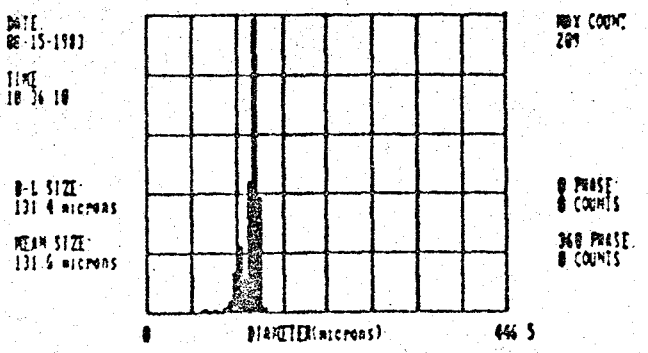

Figure 45 - Pinhole effect test: 200 micrometer pinhole

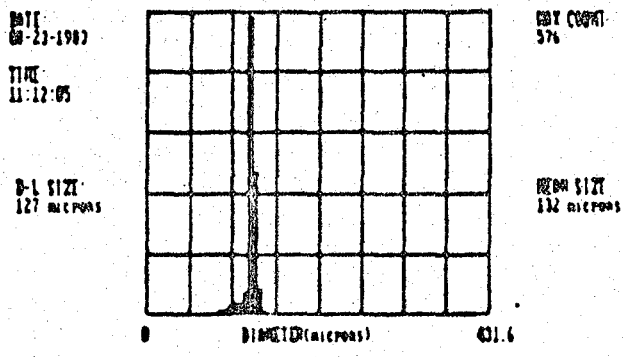

Figure 46 - Pinhole focus test: 400 micrometer pinhole in focus

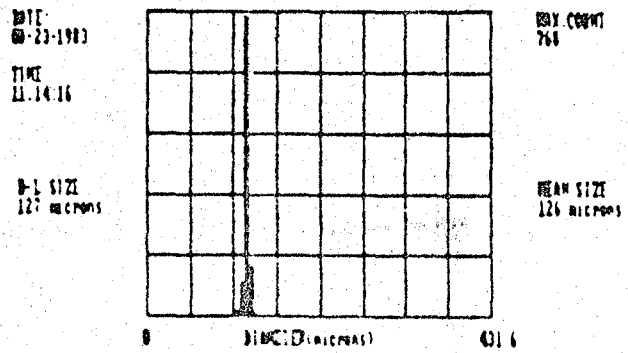

Figure 47 - Pinhole focus test: probe imaged behind pinhole

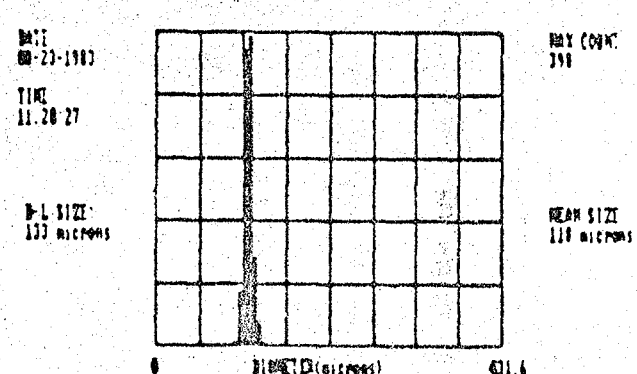

Figure 48 - Pinhole focus test: probe imaged before pinhole

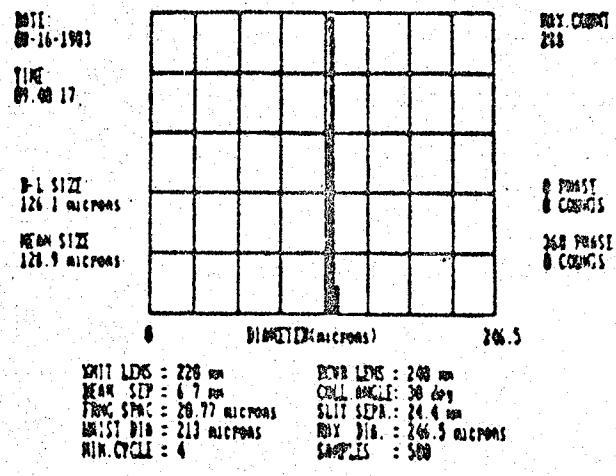

Figure 49 - Optical alignment test: probe center, reference data

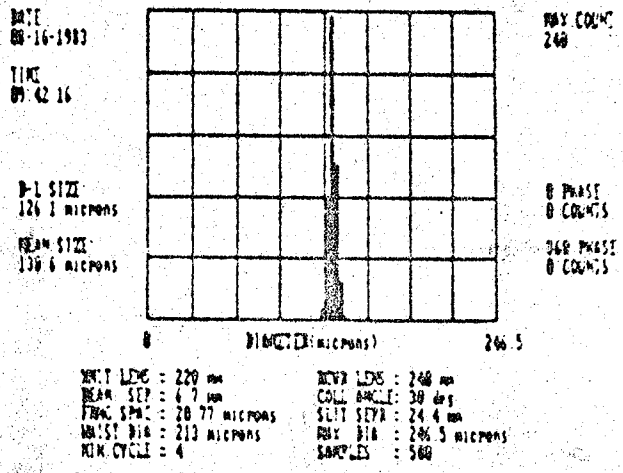

Figure 50 - Optical alignment test: probe center, pinhole removed

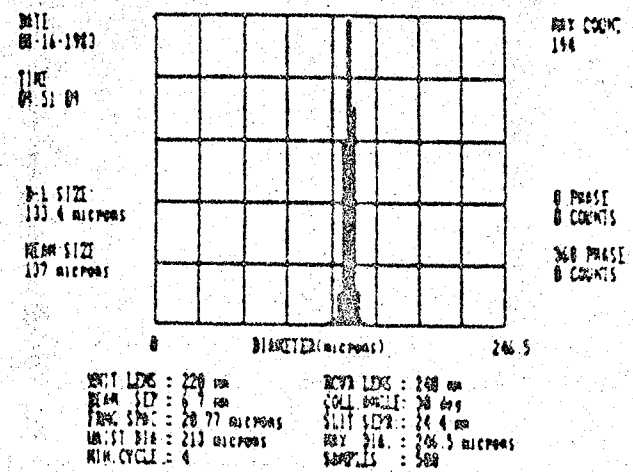

Figure 51 - Optical alignment test: 7 mm downstream of probe center

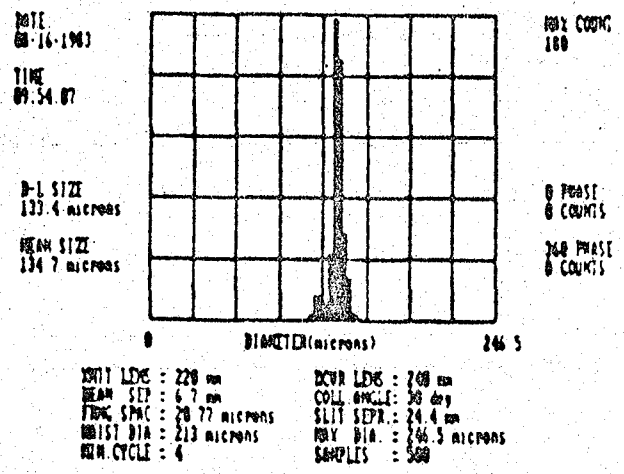

Figure 52 - Optical alignment test: 6.5 mm upstream of probe center

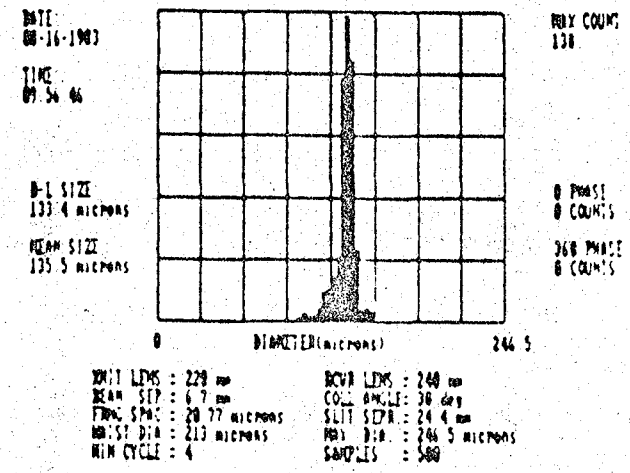

Figure 53 - Optical alignment test: nearside limit of probe

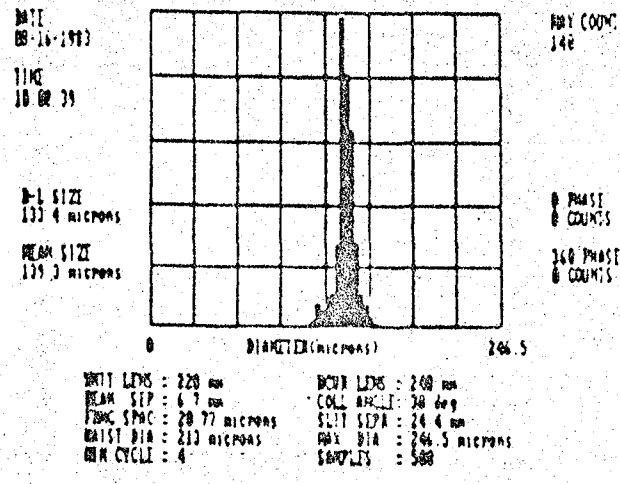

Figure 54 - Optical alignment test: farside limit of probe

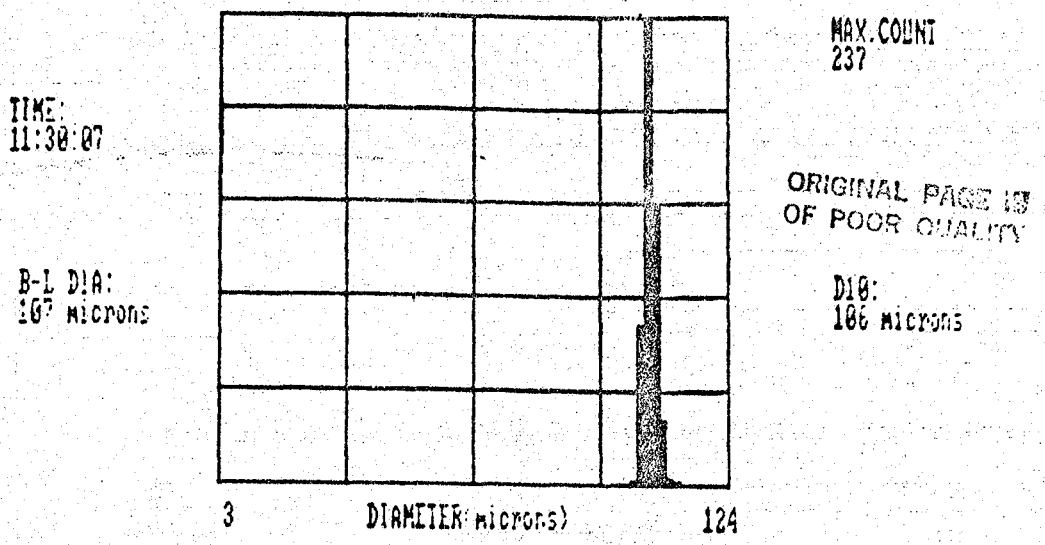

FIGURE 55 - Beam Intensity Test: Equal Beam Intensities (50:50 Ratio)

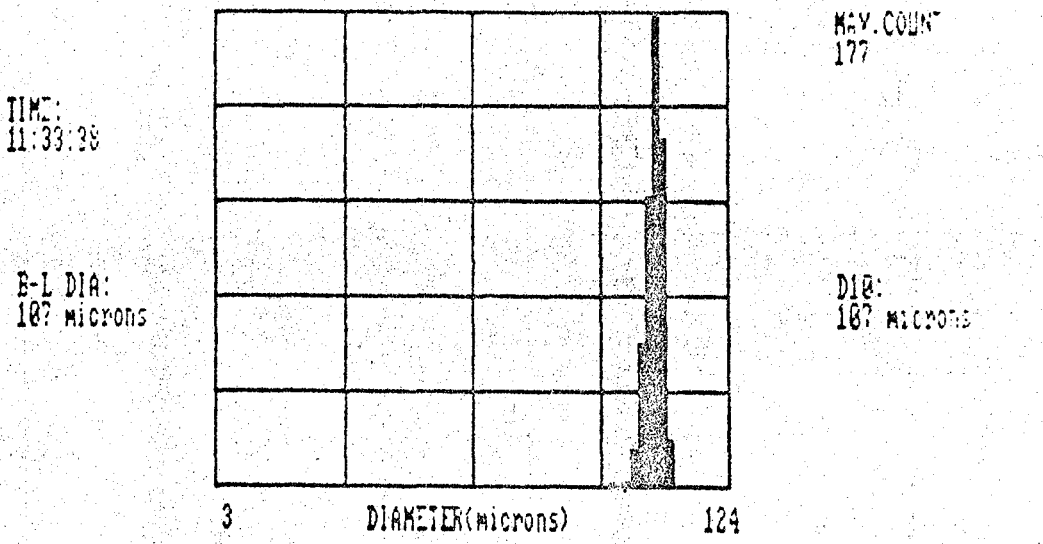

FIGURE 56 - Beam Intensity Test: One Beam Attenuated (91:9 Ratio)

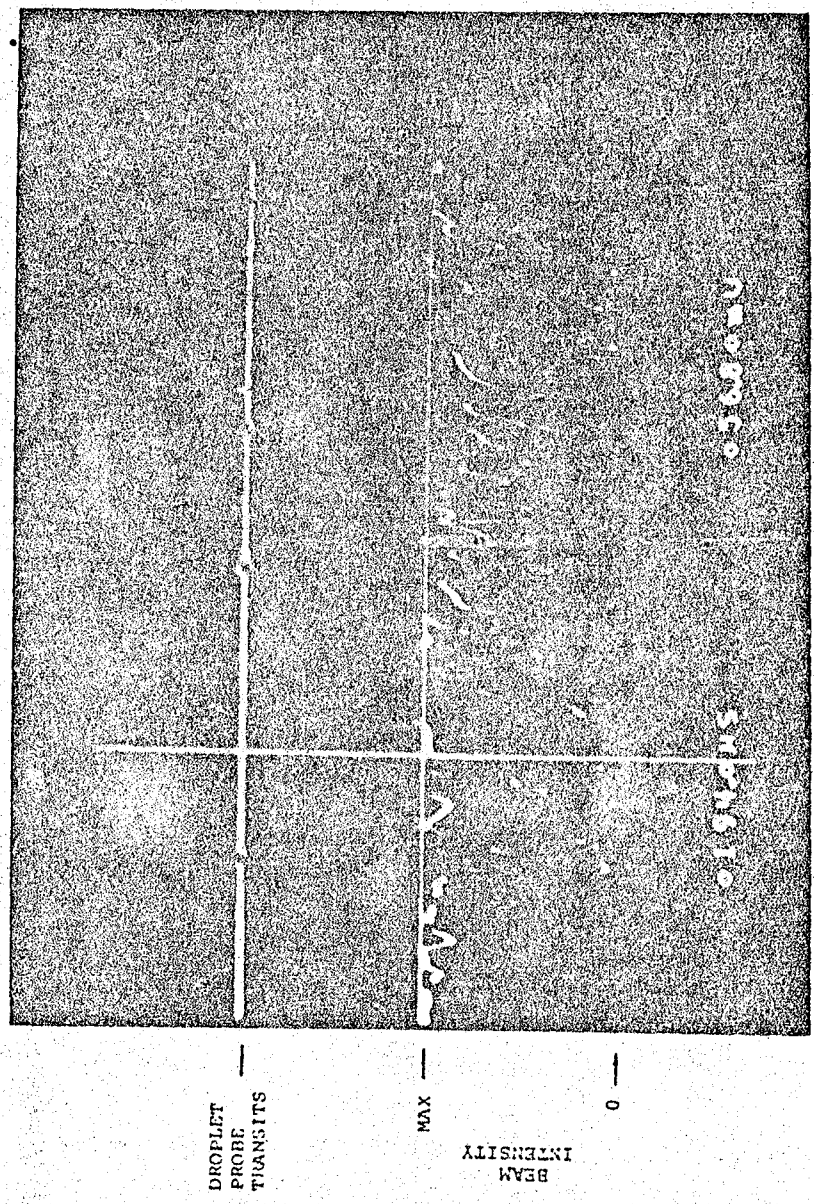

FIGURE 57 - Oscilloscope Trace Showing Beam Attenuation and Drop-out Due to Spray Interference

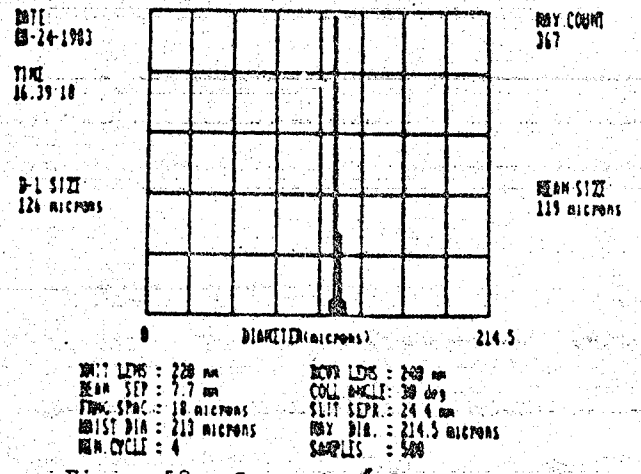

Figure 58 - Spray interference test:
monodisperse generator without spray, baseline data

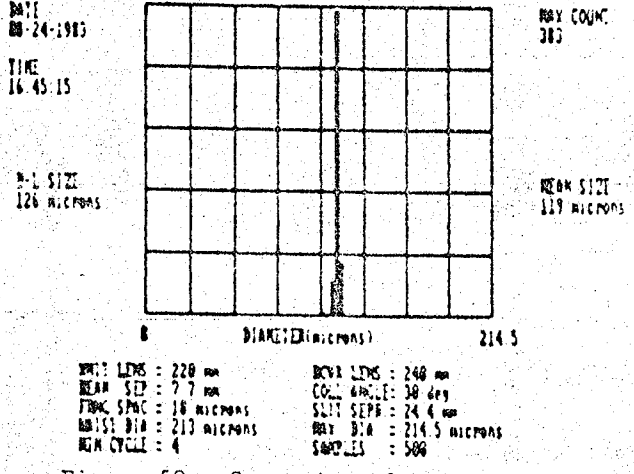

Figure 59 - Spray interference test:
40 micrometer mean drop diameter spray upstream of probe

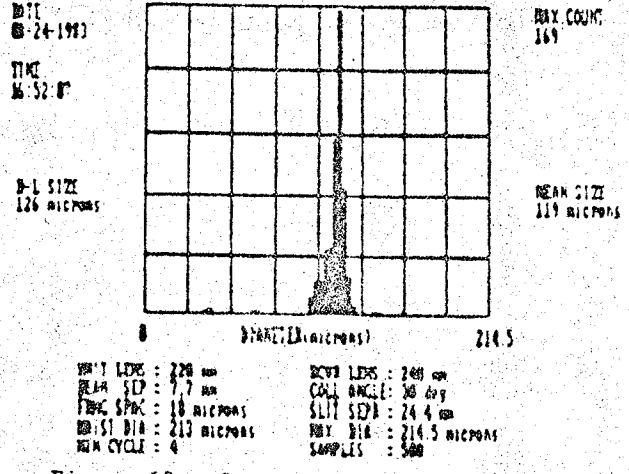

Figure 60 - Spray interference test:
100 micrometer mean drop diameter spray upstream of probe

End of Document